Applied Energy 358 (2024) 122557

Contents lists available at ScienceDirect

Applied Energy

journal homepage: www.elsevier.com/locate/apenergy

Optimal operation of multi-integrated energy system based on multi-level Nash multi-stage robust

Zongnan Zhang *, Kudashev Sergey Fedorovich

Federal State Budgetary Educational Institution of Higher Education «National Research Ogarev Mordovia State University», Bolshevistskaya str., 68, Saransk, Republic of Mordovia, 430005, Russia

HIGHLIGHTS

- An IES is proposed that incorporates multiple energy flows, with the inclusion of EHM and GHDCHP.
- A three-level Nash three-stage robust optimization model is proposed.
- An ADMM algorithm is proposed, which combines AOP-Looped C&CG.

ARTICLE INFO

Keywords:
Integrated energy system
PV prosumer
Nash-Stackelberg-Nash
Three-stage robust
Distributed optimization

ABSTRACT

To address the challenges faced by an integrated energy system (IES) during independent operation, such as high operating costs and significant uncertainties in electricity prices and source-load, a cooperative operation method based on a three-level Nash three-stage robust optimization is proposed for the Multi-integrated energy system (MIES). Firstly, the IES is enhanced by incorporating the coupling of multiple energy flows (electricity, heat, hydrogen, and gas) through the integration of an electric hydrogen module (EHM) and gas hydrogen doping combined heat and power (GHDCHP). Secondly, a Nash-Stackelberg-Nash game framework is constructed using game theory to accurately capture the interaction characteristics between the MIES and the Multi-PV prosumer (MPVP). Subsequently, a three-stage robust optimization model is developed for the IES, taking into full consideration the multiple uncertainties in electricity prices and source-load. This model is coupled with the Nash-Stackelberg-Nash game to propose a three-level Nash three-stage robust optimization model. Additionally, an ADMM algorithm coupling AOP-Looped C&CG is proposed to effectively solve the model. Finally, the effectiveness of the proposed method is validated through numerical examples.

1. Introduction

The trends of multi-energy flow coupling and clean substitution are driving forces for the future development of energy systems, leading to a transformation of common user in the energy system into “PV prosumer”. The IES with electricity, heat, hydrogen, and gas will be the most significant form of energy system. Moreover, cooperative operation of the MIES can effectively enhance energy utilization efficiency. However, the multiple uncertainties in electricity prices and source-load, as well as the conflicts of interest among MIESs, pose significant challenges for modeling, planning, and operation.

Hydrogen, as a high-quality secondary energy carrier, holds significant application value in various sectors such as power generation, heating, industry, and transportation, particularly in areas where electrification and decarbonization are challenging. Hydrogen can be flexibly transferred through hydrogen storage devices and has great dispatch potential when combined with hydrogen-consuming equipment. Many scholars have conducted research on hydrogen’s involvement in system optimization and scheduling. In [1], a multi-energy complementary system of electricity, heat, and hydrogen is established, aiming to minimize system operational costs and maximize the accommodation of surplus wind power. Ref. [2] constructs an optimal investment planning model considering electrolyzer (EL) and hydrogen energy storage (HES), and synchronizes the operation of the power grid and hydrogen supply chain during the planning phase. Ref. [3] explores the synergistic optimization operation of EL, HES, and hydrogen fuel cell

* Corresponding author.
E-mail address: chinazzn1996@163.com (Z. Zhang).

https://doi.org/10.1016/j.apenergy.2023.122557
Received 13 October 2023; Received in revised form 26 November 2023; Accepted 23 December 2023
Available online 6 January 2024
0306-2619/

(HFC), which can improve the economic efficiency of the system. However, existing research lacks a comprehensive consideration of the entire process of hydrogen production, storage, and utilization. Therefore, in this study, we aggregate "EL + HES + HFC" into an EHM. Additionally, the hydrogen released from HES can be injected into natural gas to form hydrogen-doped natural gas, which serves as fuel for GHDCHP, thereby supplying energy to the system and promoting the accommodation of new energy sources.

With the growth of residential photovoltaics, traditional electricity common users are gradually transforming from consumers to PV prosumers with the capability to generate electricity. This transition enables not only the cooperative operation of MIES but also the interconnectedness and mutual support among MPVP within the IES. In such a coordinated optimization problem involving multiple entities, game theory accurately reflects the interaction characteristics among the participating entities and effectively facilitates intelligent decision-making by multiple entities. Ref. [5–7] address the two major issues of energy trading and profit allocation among different entities based on the Nash bargaining solution, while employing the Alternating Direction Method of Multipliers (ADMM) for distributed computation to ensure the privacy of each entity. Ref. [8] analyzes the supply-demand interaction relationship based on a leader-follower game model with the park operator as the leader and users as followers. Ref. [9,10] establish a peer-to-peer (P2P) transaction model based on the principles of bilateral economic dispatch, taking into account prosumers' energy preferences. However, the aforementioned studies either only consider the competitive relationship among multiple entities or solely focus on the potential for cooperation between different entities, without seeking cooperation in a competitive context. Therefore, in addition to constructing the IES and PV prosumer as a Stackelberg game, we also consider the Nash game among different IESs and PV prosumers, thereby forming a Nash-Stackelberg-Nash game, referred to as the three-level Nash game.

Furthermore, with the access of external power grids and the massive grid connection of renewable energy, the multiple uncertainties of electricity prices and source-load can impact the equilibrium of the Nash-Stackelberg-Nash game as the number of participating entities increases. Uncertainty handling methods include interval programming, stochastic programming, and robust programming. A multi-energy system scheduling model considering source-load uncertainty was constructed using interval programming in Ref. [11]. Ref. [12] developed a regional integrated energy system planning model considering source-load uncertainty through stochastic programming. Ref. [13] incorporated source-price uncertainty and utilized a particle swarm - interval linear programming method to construct a bi-level planning model, which optimized the configuration of energy storage devices and improved economic performance. Ref. [14,15] employ robust optimization to study demand response strategies for IES under electricity price uncertainty. Ref. [16,17] establish two-stage robust economic dispatch models considering source-load uncertainty within microgrids and iteratively solve them using the C&CG algorithm to obtain the optimal results under the worst-case scenario. However, the previous studies either fail to simultaneously consider the multiple uncertainties of both electricity prices and source-load or neglect the impact of uncertainty factors on the system under a game relationship. Therefore, in our study, we simultaneously consider the multiple uncertainties of electricity prices and source-load, construct a three-stage robust optimization model for the system, and couple the three-stage robust optimization with the Nash-Stackelberg-Nash game. This approach further establishes a three-level Nash three-stage robust optimization model. Additionally, we propose a distributed ADMM algorithm that combines AOP-Looped C&CG for solving the model.

To sum up, the work in this paper and previous references are compared in Table 1. For addressing these issues, we propose an IES that incorporates multiple energy flows, including electricity, heat, hydrogen, and gas, with the inclusion of EHM and GHDCHP. To accurately reflect the interaction characteristics between MIES and MPVP, we employ game theory and establish a Nash-Stackelberg-Nash game framework. Next, we fully consider the multiple uncertainties of electricity prices and source-load and construct a three-stage robust optimization model for the system. This model is then coupled with the Nash-Stackelberg-Nash game, resulting in a three-level Nash three-stage robust optimization model. To effectively solve this model, we propose an ADMM algorithm that combines AOP-Looped C&CG. Finally, the effectiveness of the proposed method is validated through case studies. The main contributions are summarized below.

1) An IES is proposed that incorporates multiple energy flows, including electricity, heat, hydrogen, and gas, with the inclusion of EHM and GHDCHP.
2) A three-level Nash three-stage robust optimization model is proposed.
3) An ADMM algorithm is proposed, which combines AOP-Looped C&CG.

2. IES framework

In this section, the architecture of MIES is presented, followed by an explanation of the energy flows within IES, the specific components of EHM, and the energy requirements of PV prosumer or common user.

The energy trading framework structure of the investigated MIES is illustrated in Fig. 1. Each IES can achieve P2P distributed energy sharing with other IES through dedicated power interconnection lines. In terms of information sharing, IES does not need to disclose all its self-related information to other IES during electricity transactions, ensuring the privacy of each IES. On the physical level, IES can share electrical energy through dedicated power interconnection lines, resolving congestion

Table 1
Comparison of the state-of-the-art references with the proposed methods.

Ref.	IES Model			Game and Robust Coupling		Distributed Optimization Algorithm	
	EHM	GHDCHP	PV Prosumer/Common User	Game	Robust	AOP-Looped C&CG Algorithm	ADMM
[2]	EL、HES	×	×	×	×	×	×
[3]	√	×	×	×	×	×	×
[4]	EL	√	×	×	×	×	×
[5–7]	×	×	×	Nash Game	×	×	√
[8]	×	×	×	Stackelberg Game	×	×	×
[9,10]	×	×	√	Nash Game	×	×	√
[14,15]	HES、HFC	×	×	×	Uncertainty in Electricity Prices	HS Algorithm/ Strong Duality	×
[16,17]	×	×	×	×	Source and Load Uncertainty	C&CG	×
[23]	×	×	×	Stackelberg Game	Source and Load Uncertainty	C&CG	×
[24]	×	×	×	×	×	√	×
Proposed	√	√	√	Nash-Stackelberg-Nash Game	Electricity Price and Source-Load Uncertainty	√	√

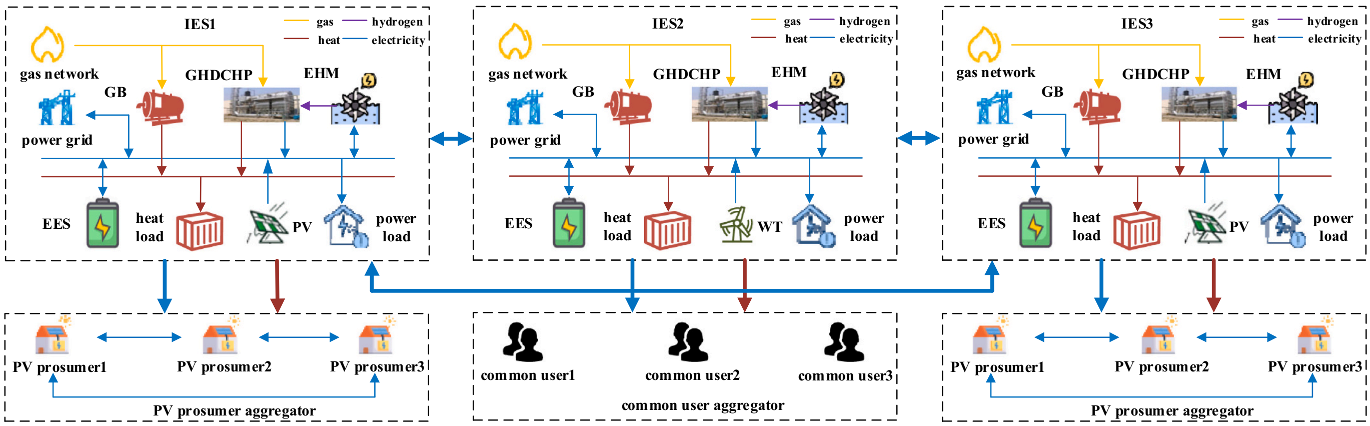

Fig. 1. MIES architecture.

issues at the public busbar and improving the overall operational efficiency of multiple IES. Additionally, as the energy-supplying side, IES interacts bidirectionally with PV prosumer aggregator or common user aggregator on the energy-consuming side. This enhances the benefits of the energy-supplying side and the consumer surplus of the energy-consuming side. Moreover, within the PV prosumer aggregator, PV prosumer can share centralized electrical energy with other PV prosumer through dedicated power interconnection lines, effectively improving the electricity utilization efficiency of PV prosumer.

Within the IES, multiple heterogeneous energy sources (electricity, heat, gas, and hydrogen) are integrated. Renewable energy devices include WT and PV, energy conversion devices include gas boiler (GB), GHDCHP, and EHM. Energy storage device include electric energy storage (EES), and load encompass both electric and thermal load. The IES is also connected to external power grid and gas network, providing electricity and heat to PV prosumer or common user to meet their energy demand.

The EHM is composed of EL, HES, and HFC, as shown in Fig. 2. Within the EHM, hydrogen gas generated by the electrolysis of water in EL is stored in HES when the EHM is being charged, operating in a power-to-hydrogen (P2H) mode. Conversely, during discharge, HFC consumes the hydrogen gas released from HES to generate electricity, operating in a hydrogen-to-power (H2P) mode. Notably, P2H and H2P operations do not occur simultaneously within the EHM.

3. IES modeling and planning framework

In this section, the conceptual framework of the three-stage robust planning model for IES is first introduced, along with the modeling approach for uncertainty. Next, the bi-level Nash planning framework for PV prosumer is presented, along with the modeling approach for bi-level Nash. Finally, the three-level Nash three-stage robust planning framework for three IESs is introduced, along with the modeling approach for three-level Nash and the coupling of three-stage robust.

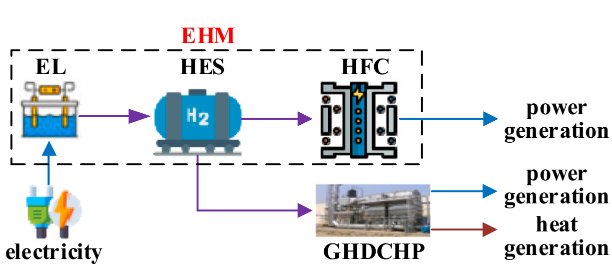

Fig. 2. EHM architecture.

3.1. IES three-stage robust planning framework

The framework of the three-stage robust planning model for IES is depicted in Fig. 3, and the objective function can be expressed as (1). The goal of this model is to minimize the scheduling and operation cost of the IES. Specifically, the first-stage decision determines the operation plan to mitigate the uncertainty in electricity price and source-load. The second-stage involves searching for scenario that maximize the system's minimum purchasing and selling electricity cost within the uncertain set of electricity price, given the first-stage decision. The third-stage involves searching for scenario that maximize the system's minimum purchasing gas and EES utilization cost within the uncertain set of source-load, given the decision from the first and second stage.

$$\min_{x\in X}\left\{\begin{array}{c}\overbrace{C^{\text{state}}}^{1\text{st}-\text{stage optimization}}+\\ \max_{v\in V}\left[\begin{array}{c}\min_{y\in Y}\overbrace{C^{\text{grid}}}^{2\text{nd}-\text{stage optimization}}+\\ \max_{u\in U}\left(\min_{z\in Z}\overbrace{\left(C^{\text{gas}}+C^{\text{ees}}\right)}^{3\text{rd}-\text{stage optimization}}\right)\end{array}\right]\end{array}\right\} \tag{1}$$

1) 1st-stage optimization

In (2), the variable $\boldsymbol{x}$ represents all scheduling and operation state variables (including the purchasing and selling electricity states $\boldsymbol{\mu}^{\text{buy}}$, $\boldsymbol{\mu}^{\text{sell}}$; the charging and discharging states of EES $\boldsymbol{\mu}^{\text{ch}}, \boldsymbol{\mu}^{\text{dis}}$; and the operating states of EHM $\boldsymbol{I}^{\text{P2H}}, \boldsymbol{I}^{\text{H2P}}$), with specific elements as follows:

$$\boldsymbol{x}=\left(\boldsymbol{I}^{\text{P2H}},\boldsymbol{I}^{\text{H2P}},\boldsymbol{\mu}^{\text{ch}},\boldsymbol{\mu}^{\text{dis}},\boldsymbol{\mu}^{\text{buy}},\boldsymbol{\mu}^{\text{sell}}\right),\boldsymbol{x}\in\{0,1\} \tag{2}$$

2) 2nd-stage optimization

After the first-stage decision, the second stage employs a robust optimization approach to minimize the system's purchasing and selling electricity cost. In (5), a polyhedral uncertainty set is constructed considering the impact of uncertain electricity price within the system. Additionally, the robust optimization method utilizes a "max-min" structure to handle price fluctuation. Specifically, the "max" obtains the worst-case scenario from the uncertain set of electricity price, resulting in the maximum purchasing and selling electricity cost for the system. The "min" obtains the worst-case scenario for the system's purchasing and selling electricity plan. In (1), $\boldsymbol{v}$ represents the uncertain variable of electricity price (including the purchasing price $\widetilde{\boldsymbol{p}}^{\text{buy}}$ and selling price $\widetilde{\boldsymbol{p}}^{\text{sell}}$), as shown in (3); $\boldsymbol{y}$ represents the purchasing and selling electricity plan (including the purchase quantity $\boldsymbol{P}^{\text{buy}}$ and sale quantity $\boldsymbol{P}^{\text{sell}}$), as

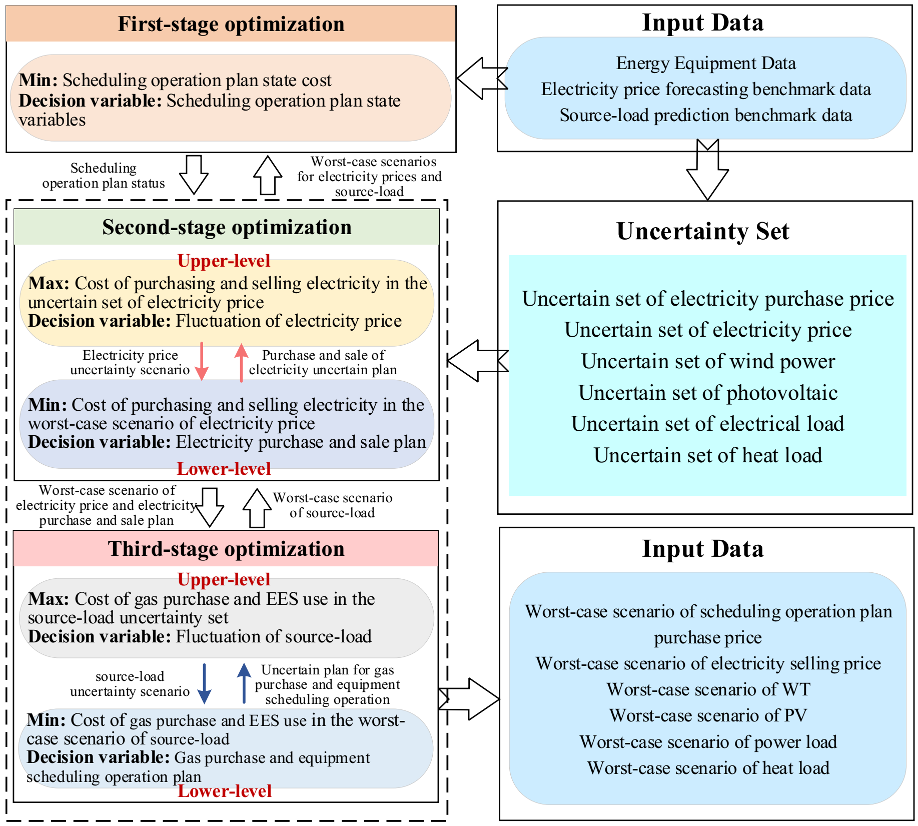

Fig. 3. IES three-stage robust programming model framework.

shown in (4).

$$\boldsymbol{v} = \left(\widetilde{\boldsymbol{p}}^{\mathrm{buy}}, \widetilde{\boldsymbol{p}}^{\mathrm{sell}}\right) \tag{3}$$

$$\boldsymbol{y} = \left(\boldsymbol{P}^{\mathrm{buy}}, \boldsymbol{P}^{\mathrm{sell}}\right) \tag{4}$$

$$V^{\mathrm{buy}} = \left\{ \widetilde{\boldsymbol{p}}^{\mathrm{buy}} \middle| \begin{array}{c} \widetilde{p}_t^{\mathrm{buy}} = \widehat{p}_t^{\mathrm{buy}} + \\ p_t^{\mathrm{buy}+}\pi_t^{\mathrm{buy}+} - \\ p_t^{\mathrm{buy}-}\pi_t^{\mathrm{buy}-}, \\ \pi_t^{\mathrm{buy}+/-} \in \{0,1\}, \\ \sum_t \left(\pi_t^{\mathrm{buy}+} + \pi_t^{\mathrm{buy}-}\right) \leqslant \Gamma^{\mathrm{buy}} \end{array} \right\} \forall t \tag{5}$$

In (5), $\widetilde{p}_t^{\mathrm{buy}}, \widehat{p}_t^{\mathrm{buy}}, p_t^{\mathrm{buy}+}, p_t^{\mathrm{buy}-}$ correspond to the actual value, predicted value, upper deviation value, and lower deviation value of the purchasing price, respectively. Similarly, $\pi_t^{\mathrm{buy}+}, \pi_t^{\mathrm{buy}-}$ represent the state variable for the upper and lower deviation of the purchasing price. The uncertainty budget, denoted as Γ^{buy}, represents the uncertainty level of the purchasing price and is an integer with a maximum value of one scheduling period T. A higher value of Γ^{buy} indicates a greater number of time periods with system uncertainty and hence stronger robustness.

Remark 1. The polyhedral uncertainty set for the purchasing price is constructed here, and the same approach is applied to the uncertainty set for the selling price, which will not be further elaborated.

3) 3rd-stage optimization

After the first and second-stage decisions, the third stage also employs a robust optimization approach to minimize the system's purchasing gas and EES utilization cost. Similarly, the uncertainty of source-load within the system is described using polyhedral uncertainty set. In (1), $\boldsymbol{u}$ represents the uncertain variable of source-load (including wind power $\widetilde{\boldsymbol{P}}^{\mathrm{WT}}$, photovoltaic $\widetilde{\boldsymbol{P}}^{\mathrm{PV}}$, electrical load $\widetilde{\boldsymbol{P}}_e^{\mathrm{load}}$, and thermal load $\widetilde{\boldsymbol{P}}_h^{\mathrm{load}}$), as shown in (6). The variable z represents the purchasing gas and equipment scheduling operation plan, as shown in (7).

$$\boldsymbol{u} = \left(\widetilde{\boldsymbol{P}}^{\mathrm{WT}}, \widetilde{\boldsymbol{P}}^{\mathrm{PV}}, \widetilde{\boldsymbol{P}}_e^{\mathrm{load}}, \widetilde{\boldsymbol{P}}_h^{\mathrm{load}}\right) \tag{6}$$

$$\boldsymbol{z} = \left(\begin{array}{c} \boldsymbol{P}_e^{\mathrm{CHP}}, \boldsymbol{P}_{h,\mathrm{water}}^{\mathrm{CHP}}, \boldsymbol{P}_{h,\mathrm{smoke}}^{\mathrm{CHP}}, \boldsymbol{P}_h^{\mathrm{CHP}}, \boldsymbol{GAS}_{\mathrm{Ing}}^{\mathrm{CHP}}, \boldsymbol{GAS}_{\mathrm{H_2}}^{\mathrm{CHP}}, \\ \boldsymbol{P}^{\mathrm{P2H}}, \boldsymbol{H}^{\mathrm{we}}, \boldsymbol{P}^{\mathrm{H2P}}, \boldsymbol{H}^{\mathrm{fc}}, \boldsymbol{S}^{\mathrm{HES}}, \\ \boldsymbol{P}_h^{\mathrm{GB}}, \boldsymbol{GAS}^{\mathrm{GB}}, \\ \boldsymbol{P}^{\mathrm{ch}}, \boldsymbol{P}^{\mathrm{dis}}, \boldsymbol{S}^{\mathrm{EES}} \end{array} \right) \tag{7}$$

In (7), the following variables are defined:$\boldsymbol{P}_e^{\mathrm{CHP}}$: Power generation capacity of GHDCHP; $\boldsymbol{P}_{h,\mathrm{water}}^{\mathrm{CHP}}$: Heat recovery capacity from hot water circulation of GHDCHP; $\boldsymbol{P}_{h,\mathrm{smoke}}^{\mathrm{CHP}}$: Heat recovery capacity from flue gas of GHDCHP; $\boldsymbol{P}_h^{\mathrm{CHP}}$: Heat production capacity of GHDCHP; $\boldsymbol{GAS}_{\mathrm{Ing}}^{\mathrm{CHP}}$: Natural gas consumption of GHDCHP; $\boldsymbol{GAS}_{\mathrm{H_2}}^{\mathrm{CHP}}$: Hydrogen consumption of GHDCHP; $\boldsymbol{P}^{\mathrm{P2H}}$: Electric power consumption of EHM under P2H operation mode; $\boldsymbol{H}^{\mathrm{we}}$: Hydrogen production mass of EHM under P2H operation mode; $\boldsymbol{P}^{\mathrm{H2P}}$: Power generation capacity of EHM under H2P operation mode; $\boldsymbol{H}^{\mathrm{fc}}$: Hydrogen consumption mass of EHM under H2P operation mode; $\boldsymbol{S}^{\mathrm{HES}}$: Hydrogen storage capacity of EHM's HES; $\boldsymbol{P}_h^{\mathrm{GB}}$: Heat production capacity of GB; $\boldsymbol{GAS}^{\mathrm{GB}}$: Natural gas consumption of GB; $\boldsymbol{P}^{\mathrm{ch}}$: Charging power of EES; $\boldsymbol{P}^{\mathrm{dis}}$: Discharging power of EES; $\boldsymbol{P}^{\mathrm{dis}}$: Energy storage capacity of EES.

Remark 2. The form of the uncertainty set for source-load is the same as that for the purchasing price, and will not be further elaborated.

3.2. PV prosumer bi-level Nash programming framework

The framework of the PV prosumer bi-level Nash planning model is illustrated in Fig. 4. The model consists of two stages. In the first stage, there is a Stackelberg game between the IES and the PV prosumer aggregator. The energy price formulated by the IES are adjusted based on the energy purchase demand provided by the PV prosumer aggregator, aiming to maximize its own benefits. These formulated energy price are then transmitted to the second stage. In the second stage, a Nash game model is applied among the members of the PV prosumer aggregator [18]. Moreover, the objective function of the PV prosumer aggregator can be expressed in (8). Based on the electricity price calculated in the first stage, appropriate levels of interactive electricity quantity and price among PV prosumers are determined to ensure that, on the premise of maximizing cooperative benefits, each PV prosumer can profit through collaboration. The PV prosumer aggregator then sends the energy purchase demand from the PV prosumer back to the IES in the first stage.

$$\min_{q\in Q}\left(C^{\text{tran}}+C^{\text{dr}}\right) \tag{8}$$

In (8), $\boldsymbol{q}$ represents the variable for PV prosumer scheduling and operational plan, including reducible electricity and heat load $\boldsymbol{p}^{\text{cut}},\boldsymbol{h}^{\text{cut}}$, purchased electricity and heat $\boldsymbol{p}^{\text{load}}$, $\boldsymbol{h}^{\text{load}}$, and interactive electricity quantity $\boldsymbol{p}^{\text{tran}}$. The specific elements are as follows:

$$\boldsymbol{q}=\left(\begin{array}{c}\boldsymbol{p}_1^{\text{cut}},\boldsymbol{h}_1^{\text{cut}},\boldsymbol{p}_1^{\text{load}},\boldsymbol{h}_1^{\text{load}},\\ \boldsymbol{p}_2^{\text{cut}},\boldsymbol{h}_2^{\text{cut}},\boldsymbol{p}_2^{\text{load}},\boldsymbol{h}_2^{\text{load}},\\ \boldsymbol{p}_3^{\text{cut}},\boldsymbol{h}_3^{\text{cut}},\boldsymbol{p}_3^{\text{load}},\boldsymbol{h}_3^{\text{load}},\\ \boldsymbol{p}_{12}^{\text{tran}},\boldsymbol{p}_{13}^{\text{tran}},\boldsymbol{p}_{23}^{\text{tran}}\end{array}\right) \tag{9}$$

Remark 3. For common user, there is only a Stackelberg game between the IES and the common user aggregator, and there is no Nash game involving the common user aggregator.

3.3. Three IES three-level Nash three-stage robust planning framework

The framework of the three-level Nash planning model is illustrated in Fig. 5. The framework of the three-level Nash three-stage robust planning model for three IESs is illustrated in Fig. 6. The first level Nash game represents the Nash game among the three PV prosumers. The second level Nash game represents the Stackelberg game between the IES and the PV prosumer aggregator. The third level Nash game represents the Nash game among the three IESs. Additionally, each IES constructs a three-stage robust planning model [19–21]. In [7], it has been proved that the Nash bargaining model of cooperative game can be equivalent to solving the subproblem P1 of maximizing cooperation benefit and the subproblem P2 of energy transaction payment. For P1, the decision model for the i-th IES can be formulated as (10).

$$\min_{x\in X,w\in W}\left\{\begin{array}{c}C^{\text{state}}-C^{\text{tran}}+\\ \sum_t\sum_{j\in J,j\neq i}\left[\begin{array}{c}\lambda_{ij,1,t}\left(P^e_{ij,t}+P^e_{ji,t}\right)+\\ \frac{\rho_{ij,1}}{2}\left\|P^e_{ij,t}+P^e_{ji,t}\right\|_2^2\end{array}\right]\end{array}\right\}+\max_{v\in V}\min_{y\in Y}C^{\text{grid}}+\max_{u\in U}\min_{z\in Z}\left(C^{\text{gas}}+C^{\text{ees}}\right) \tag{10}$$

In (10), $\lambda_{ij,1,t}$ is the Lagrange multiplier, $\rho_{ij,1}$ is the penalty factor, and $\boldsymbol{w}$ represents the energy price (including electricity price $\boldsymbol{p}^e$ and heat price $\boldsymbol{p}^h$) determined by the i-th IES for the three PV prosumers, with specific elements as follows:

$$\boldsymbol{w}=\left(\boldsymbol{p}_1^e,\boldsymbol{p}_1^h,\boldsymbol{p}_2^e,\boldsymbol{p}_2^h,\boldsymbol{p}_3^e,\boldsymbol{p}_3^h\right) \tag{11}$$

For P2, the decision model for the i-th IES can be formulated as (12).

$$\min\left\{\begin{array}{c}-\ln\left(C_i^0-C_i^*+\sum_t\sum_{j\in J,j\neq i}p^e_{ij,t}P^e_{ij,t}\right)+\\ \sum_t\sum_{j\in J,j\neq i}\left[\begin{array}{c}\lambda_{ij,2,t}\left(p^e_{ij,t}-p^e_{ji,t}\right)+\\ \frac{\rho_{ij,2}}{2}\left\|p^e_{ij,t}-p^e_{ji,t}\right\|_2^2\end{array}\right]\end{array}\right\} \tag{12}$$

In (12), $\lambda_{ij,2,t}$ is the Lagrange multiplier, $\rho_{ij,2}$ is the penalty factor, C_i^0 represents the cost for the i-th IES when not participating in electricity trading, which can be obtained by solving the optimization problem with the transaction quantity set to 0, and C_i^* denotes the optimal cost obtained by the i-th IES when solving the P1.

Remark 4. The cooperative game Nash bargaining model among PV prosumer aggregator members can equivalently be solved by maximizing cooperative benefit and energy transaction payment, as shown in (A1)–(A2).

4. Formulation of three-level Nash three-stage robust programming model

The mathematical formulations of the proposed three-level Nash three-stage robust planning model are presented in this section.

4.1. Objective function

1) IES scheduling operation plan state cost

$$C^{\text{state}}=\alpha_{\text{HES}}\sum_t\left(\alpha_{\text{P2H}}I_t^{\text{P2H}}+\alpha_{\text{H2P}}I_t^{\text{H2P}}\right)+\beta_{\text{EES}}\sum_t\left(\mu_t^{\text{ch}}+\mu_t^{\text{dis}}\right)+\gamma_{\text{grid}}\sum_t\left(\mu_t^{\text{buy}}+\mu_t^{\text{sell}}\right) \tag{13}$$

In (13), $\alpha_{\text{HES}},\alpha_{\text{P2H}},\alpha_{\text{H2P}}$ represent the price coefficients for the operational states of the EHM, β_{EES} represents the price coefficient for the charging and discharging states of the EES, and γ_{grid} represents the price coefficient for the buying and selling states of electricity.

2) Electricity purchase and sale cost of IES

$$C^{\text{grid}}=\sum_t\left(p_t^{\text{buy}}P_t^{\text{buy}}-p_t^{\text{sell}}P_t^{\text{sell}}\right) \tag{14}$$

In (14), p_t^{buy} represents the purchasing price of electricity, and p_t^{sell} represents the selling price of electricity.

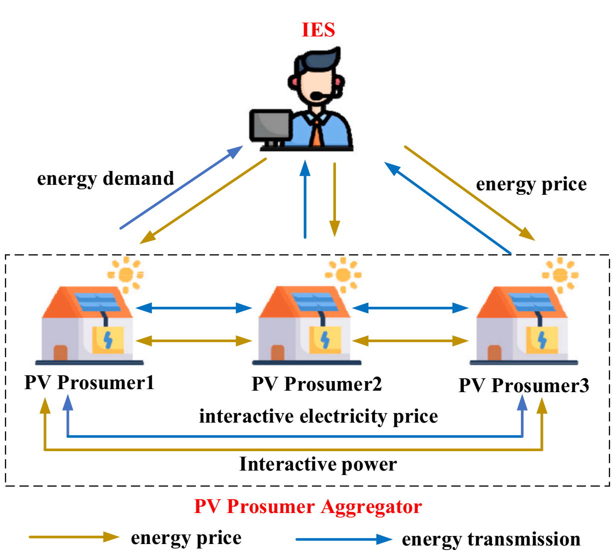

Fig. 4. PV prosumer bi-level Nash programming model framework.

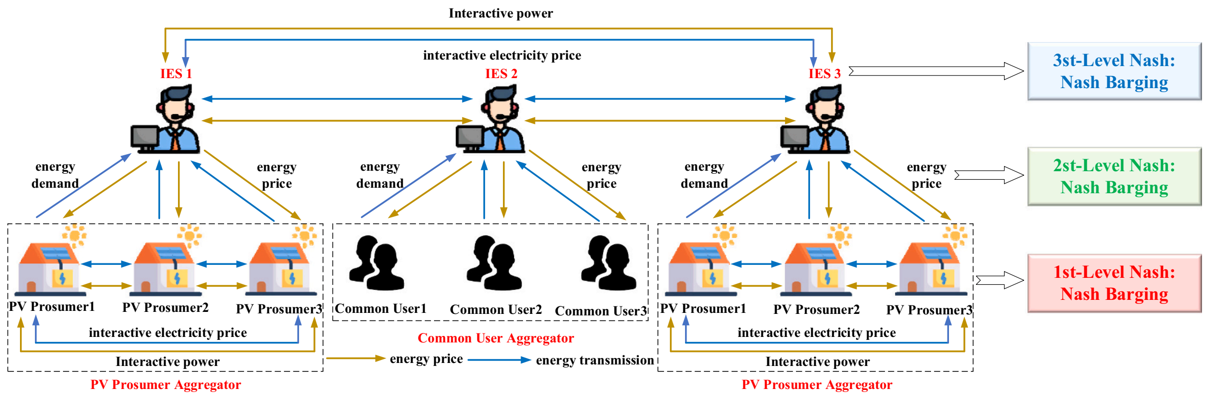

Fig. 5. Three-level Nash programming model framework.

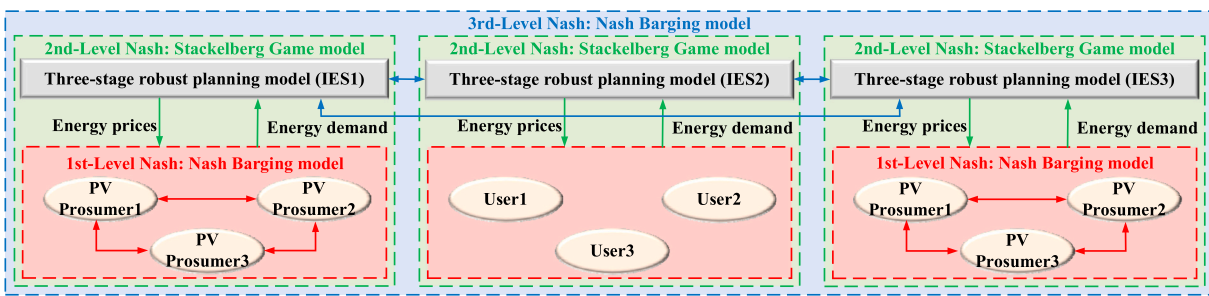

Fig. 6. Three IES three-level Nash three-stage robust programming model framework

3) Gas purchasing cost of IES

$$C^{gas} = p^{gas}\sum_t \left(GAS_{Ing,t}^{CHP} + GAS_t^{GB}\right) \tag{15}$$

In (15), p^{gas} represents the price of natural gas.

4) EES utilization cost of IES

$$C^{ees} = \alpha_{EES}\sum_t \left(P_t^{ch} + P_t^{dis}\right) \tag{16}$$

In (16), α_{EES} represents the cost coefficient for the utilization of the EES.

5) PV prosumer aggregator energy purchase cost

$$C^{tran} = \sum_t \begin{pmatrix} p_{1,t}^e p_{1,t}^{load} + p_{1,t}^h h_{1,t}^{load} + \\ p_{2,t}^e p_{2,t}^{load} + p_{2,t}^h h_{2,t}^{load} + \\ p_{3,t}^e p_{3,t}^{load} + p_{3,t}^h h_{3,t}^{load} \end{pmatrix} \tag{17}$$

6) Demand response cost of PV prosumer aggregator or common user aggregator

$$C^{dr} = \alpha_{cut}^e \sum_t \left(p_{1,t}^{cut} + p_{2,t}^{cut} + p_{3,t}^{cut}\right) + \alpha_{cut}^h \sum_t \left(h_{1,t}^{cut} + h_{2,t}^{cut} + h_{3,t}^{cut}\right) \tag{18}$$

In (18), α_{cut}^e represents the penalty coefficient for reducible electric load, while α_{cut}^h represents the penalty coefficient for reducible heat load.

4.2. Constraints

1) Electricity Transaction Constraints with Power Gird

$$0 \leqslant P_t^{buy} \leqslant \mu_t^{buy} P_{max}^{buy} \tag{19}$$

$$0 \leqslant P_t^{sell} \leqslant \mu_t^{sell} P_{max}^{sell} \tag{20}$$

$$\mu_t^{buy} + \mu_t^{sell} \leqslant 1 \tag{21}$$

2) Operational Constraints of GHDCHP

$$P_{e,t}^{CHP} = \alpha_1^{CHP} GAS_{Ing,t}^{CHP} + \alpha_2^{CHP} GAS_{H_2,t}^{CHP} \tag{22}$$

$$P_{h,water,t}^{CHP} = \alpha_3^{CHP} GAS_{Ing,t}^{CHP} - \alpha_4^{CHP} GAS_{H_2,t}^{CHP} \tag{23}$$

$$P_{h,smoke,t}^{CHP} = \alpha_5^{CHP} GAS_{Ing,t}^{CHP} + \alpha_6^{CHP} GAS_{H_2,t}^{CHP} \tag{24}$$

$$P_{h,t}^{CHP} = P_{h,water,t}^{CHP} + \alpha_7^{CHP} P_{h,smoke,t}^{CHP} \tag{25}$$

$$\kappa_t = GAS_{H_2,t}^{CHP} \Big/ \left(GAS_{Ing,t}^{CHP} + GAS_{H_2,t}^{CHP}\right) \tag{26}$$

$$0 \leqslant \kappa_t \leqslant 20\% \tag{27}$$

$$0 \leqslant P_{e,t}^{CHP} \leqslant P_{e,max}^{CHP} \tag{28}$$

In (22)–(27), κ_t represents the hydrogen blending ratio of natural gas, while α_{1-7}^{CHP} represents the operational coefficient of the GHDCHP.

3) Operational Constraints of EHM

$$H_t^{we} = \alpha_1^{EHM} P_t^{P2H} \tag{29}$$

$$P_t^{H2P} = \alpha_2^{EHM} H_t^{fc} \tag{30}$$

$$I_t^{P2H} P_{min}^{P2H} \leqslant P_t^{P2H} \leqslant I_t^{P2H} P_{max}^{P2H} \tag{31}$$

$$I_t^{H2P} P_{min}^{H2P} \leqslant P_t^{H2P} \leqslant I_t^{H2P} P_{max}^{H2P} \tag{32}$$

$$I_t^{P2H} + I_t^{H2P} \leqslant 1 \tag{33}$$

$$S_t^{HES} = S_{t-1}^{HES} + H_t^{we} - H_t^{fc} - \rho_{H_2} GAS_{H_2,t}^{CHP} \tag{34}$$

$$S_0^{\mathrm{HES}} = S_{\mathrm{ini}}^{\mathrm{HES}} \tag{35}$$

$$S_T^{\mathrm{HES}} = S_0^{\mathrm{HES}} \tag{36}$$

$$S_{\min}^{\mathrm{HES}} \leqslant S_t^{\mathrm{HES}} \leqslant S_{\max}^{\mathrm{HES}} \tag{37}$$

In (29)–(30), $\alpha_{1-2}^{\mathrm{EHM}}$ represents the operational coefficient of the EHM. In (34), ρ_{H_2} represents the density of H_2.

4) Operational Constraints of GB

$$P_{h,t}^{\mathrm{GB}} = \alpha^{\mathrm{GB}} GAS_t^{\mathrm{GB}} \tag{38}$$

$$0 \leqslant P_{h,t}^{\mathrm{GB}} \leqslant P_{h,max}^{\mathrm{GB}} \tag{39}$$

In (38), α^{GB} represents the operational coefficient of the GB.

5) Operational Constraints of EES

$$0 \leqslant P_t^{\mathrm{ch}} \leqslant \mu_t^{\mathrm{ch}} P_{\max}^{\mathrm{ch}} \tag{40}$$

$$0 \leqslant P_t^{\mathrm{dis}} \leqslant \mu_t^{\mathrm{dis}} P_{\max}^{\mathrm{dis}} \tag{41}$$

$$\mu_t^{\mathrm{ch}} + \mu_t^{\mathrm{dis}} \leqslant 1 \tag{42}$$

$$S_t^{\mathrm{EES}} = S_{t-1}^{\mathrm{EES}} + \eta_{\mathrm{ch}} P_t^{\mathrm{ch}} - P_t^{\mathrm{dis}} / \eta_{\mathrm{dis}} \tag{43}$$

$$S_{24}^{\mathrm{EES}} = S_0^{\mathrm{EES}} \tag{44}$$

$$S_{\min}^{\mathrm{EES}} \leqslant S_t^{\mathrm{EES}} \leqslant S_{\max}^{\mathrm{EES}} \tag{45}$$

6) Energy Interaction Constraints

$$P_{ij,min}^{e} \leqslant P_{ij,t}^{e} \leqslant P_{ij,max}^{e} \tag{46}$$

$$p_{ij,min}^{\mathrm{tran}} \leqslant p_{ij,t}^{\mathrm{tran}} \leqslant p_{ij,max}^{\mathrm{tran}} \tag{47}$$

7) Energy Price Constraints

$$p_t^{\mathrm{pre,sell}} \leqslant p_{ij,t}^{e} \leqslant p_t^{\mathrm{pre,buy}} \tag{48}$$

$$p_t^{\mathrm{pre,sell}} \leqslant p_{ij,t}^{e,\mathrm{tran}} \leqslant p_t^{\mathrm{pre,buy}} \tag{49}$$

$$p_t^{\mathrm{pre,sell}} \leqslant p_{i,t}^{e} \leqslant p_t^{\mathrm{pre,buy}} \tag{50}$$

$$\mathrm{mean}\left(p_{i,t}^{e}\right) \leqslant p_{i,\mathrm{mean}}^{e} \tag{51}$$

$$p_{i,min}^{h} \leqslant p_{i,t}^{h} \leqslant p_{i,max}^{h} \tag{52}$$

$$\mathrm{mean}\left(p_{i,t}^{h}\right) \leqslant p_{i,\mathrm{mean}}^{h} \tag{53}$$

In (48)–(50), $p_t^{\mathrm{pre,buy}}$ represents the purchasing price of electricity from the grid, $p_t^{\mathrm{pre,sell}}$ represents the selling price of electricity to the grid, and $p_{ij,t}^{e,\mathrm{tran}}$ represents the price of electricity exchanged between PV prosumers.

8) Operational Constraints of PV prosumer

$$0 \leqslant p_{i,t}^{\mathrm{cut}} \leqslant \beta_{\mathrm{cut}}^{e} p_{i,t}^{\mathrm{L}} \tag{54}$$

$$\begin{cases} \qquad \text{PV prosumer} \\ p_{i,t}^{\mathrm{load}} = p_{i,t}^{\mathrm{L}} - p_{i,t}^{\mathrm{PV}} - p_{i,t}^{\mathrm{cut}} + \sum\limits_{j \in J, j \neq i} p_{ij,t}^{\mathrm{tran}} \\ \qquad \text{commonuser} \\ \quad p_{i,t}^{\mathrm{load}} = p_{i,t}^{\mathrm{L}} - p_{i,t}^{\mathrm{PV}} - p_{i,t}^{\mathrm{cut}} \end{cases} \tag{55}$$

$$0 \leqslant h_{i,t}^{\mathrm{cut}} \leqslant \beta_{\mathrm{cut}}^{h} h_{i,t}^{\mathrm{L}} \tag{56}$$

$$h_{i,t}^{\mathrm{load}} = h_{i,t}^{\mathrm{L}} - h_{i,t}^{\mathrm{cut}} \tag{57}$$

$$0 \leqslant p_{i,t}^{\mathrm{load}} \leqslant p_{i,max}^{\mathrm{load}} \tag{58}$$

$$0 \leqslant h_{i,t}^{\mathrm{load}} \leqslant h_{i,max}^{\mathrm{load}} \tag{59}$$

In (54)–(57), β_{cut}^{e} represents the coefficient for reducible electrical load, β_{cut}^{h} represents the coefficient for reducible thermal load, and $p_{i,t}^{\mathrm{L}}$, $h_{i,t}^{\mathrm{L}}, p_{i,t}^{\mathrm{PV}}$ represent the electrical load, thermal load, and rooftop photovoltaics of the *i*-th PV prosumer, respectively.

9) Coupling Constraints

$$P_{ij,t}^{e} + P_{ji,t}^{e} = 0 \tag{60}$$

$$p_{ij,t}^{\mathrm{tran}} + p_{ji,t}^{\mathrm{tran}} = 0 \tag{61}$$

$$p_{ij,t}^{e} - p_{ji,t}^{e} = 0 \tag{62}$$

$$p_{ij,t}^{e,\mathrm{tran}} - p_{ji,t}^{e,\mathrm{tran}} = 0 \tag{63}$$

10) Energy Balance Constraints.

The electric power balance is expressed in (64).

$$\begin{aligned} & P_t^{\mathrm{buy}} - P_t^{\mathrm{sell}} + P_{e,t}^{\mathrm{CHP}} + P_t^{\mathrm{PV}} + P_t^{\mathrm{WT}} + P_t^{\mathrm{dis}} - P_t^{\mathrm{ch}} \\ & \quad = P_{e,t}^{\mathrm{load}} + P_t^{\mathrm{P2H}} - P_t^{\mathrm{H2P}} + \sum_i p_{i,t}^{\mathrm{load}} + \sum_{j \in J, j \neq i} P_{ij,t}^{e} \end{aligned} \tag{64}$$

The heating power balance is expressed in (65).

$$P_{h,t}^{\mathrm{CHP}} + P_{h,t}^{\mathrm{GB}} = P_{h,t}^{\mathrm{load}} + \sum_i h_{i,t}^{\mathrm{load}} \tag{65}$$

In (64)–(65), $P_t^{\mathrm{WT}}, P_t^{\mathrm{PV}}$ represent the output power of WT and PV, respectively. $P_{e,t}^{\mathrm{load}}, P_{h,t}^{\mathrm{load}}$, on the other hand, represent the electrical load and thermal load.

5. Solution methodology

The proposed three-level Nash three-stage robust planning model is NP-hard and cannot be solved directly. In this section, the solution process of the proposed model is presented.

5.1. Full matrix formulation

To enhance the understandability of our subsequent discussions, the three-level Nash three-stage robust planning model for the *i*-th IES is redefined in the form of a compact matrix.

$$\left\{\begin{array}{c}\underset{x\in X,w\in W}{min}\left\{\begin{array}{c}A^Tx-w^Tq+\\ \sum_t\sum_{j\in J,j\neq i}\left[\begin{array}{l}\lambda_{ij,1,t}\left(P^e_{ij,t}+P^e_{ji,t}\right)+\\ \frac{\rho_{ij,1}}{2}\left\|P^e_{ij,t}+P^e_{ji,t}\right\|_2^2\end{array}\right]\end{array}\right\}+\\ \underset{v\in V}{max}\,\underset{y\in Y}{min}v^Ty+\\ \underset{u\in U}{max}\underset{z\in Z}{min}B^Tz\\ \text{s.t.}a^Tx+b^Tw\leqslant C\\ c^Tx+d^Tv+e^Ty\leqslant D\\ f^Tx+g^Tv+h^Ty+i^Tu+j^Tz\leqslant E\\ q=\underset{q}{\text{argmin}}\left(w^Tq+Fq\right)\\ \text{s.t.}k^Tq\leqslant G\end{array}\right. \tag{66}$$

In (66), the decision variables correspond to the developed model in Section 3, and $A,B,C,D,E,F,G,a,b,c,d,e,f,g,h,i,j,k$ are coefficient matrices. In the constraint, the first row constraint is the first stage constraint, corresponding to (21), (33), (42), (46), (50)–(53); the second row constraint is the second stage constraint, corresponding to (19)–(20); the third row constraint is the third stage constraint, corresponding to (22)–(32), (34)–(41), (43)–(45), (64)–(65); the fourth and fifth row constraints are contained in the first stage constraints, which refer to the constraints of PV prosumer aggregator or common user aggregator, corresponding to (17)–(18), (47), (54)–(59).

5.2. Linearization of bilinear terms

In (66), the first stage of the model encompasses a Stackelberg game model, where the lower-level PV prosumer aggregator or common user aggregator model can be formulated as (67).

$$\left\{\begin{array}{l}\underset{q}{min}\left(w^Tq+Fq\right)\\ \text{s.t.}k^Tq\leqslant G:\delta\end{array}\right. \tag{67}$$

Since the Stackelberg game model cannot be directly solved, it is necessary to equivalently incorporate the lower-level model using KKT conditions and add them to the upper-level constraints. The KKT conditions for (67) can be expressed as (68).

$$\left\{\begin{array}{l}w^T+F+\delta k^T=0\\ 0\leqslant\left(G-k^Tq\right)\perp\delta\geqslant0\end{array}\right. \tag{68}$$

In (68), the second row constraint is a complementary relaxation constraint, which needs to be linearized by the big-M method. The linear transformed model can be represented in (69).

$$\left\{\begin{array}{l}w^T+F+\delta k^T=0\\ 0\leqslant G-k^Tq\leqslant\text{M}\nu\\ 0\leqslant\delta\leqslant\text{M}(1-\nu)\end{array}\right. \tag{69}$$

In (69), M represents a large positive value; ν is an introduced Boolean variable; δ is an introduced dual variable.

Additionally, the bilinear term w^Tq can be linearized as (70) using strong duality theory.

$$w^Tq=-\delta^TG-Fq \tag{70}$$

Thus, (66) can be transformed into (71).

$$\left\{\begin{array}{c}\underset{x\in X,w\in W}{min}\left\{\begin{array}{c}A^Tx+\delta^TG+Fq+\\ \sum_t\sum_{j\in J,j\neq i}\left[\begin{array}{l}\lambda_{ij,1,t}\left(P^e_{ij,t}+P^e_{ji,t}\right)+\\ \frac{\rho_{ij,1}}{2}\left\|P^e_{ij,t}+P^e_{ji,t}\right\|_2^2\end{array}\right]\end{array}\right\}+\\ \underset{v\in V}{max}\,\underset{y\in Y}{min}v^Ty+\\ \underset{u\in U}{max}\underset{z\in Z}{min}B^Tz\\ \text{s.t.}a^Tx+b^Tw\leqslant C\\ c^Tx+d^Tv+e^Ty\leqslant D\\ f^Tx+g^Tv+h^Ty+i^Tu+j^Tz\leqslant E\\ w^T+F+\delta k^T=0\\ 0\leqslant G-k^Tq\leqslant\text{M}\nu\\ 0\leqslant\delta\leqslant\text{M}(1-\nu)\end{array}\right. \tag{71}$$

5.3. AOP-looped C&CG algorithm

To efficiently solve the recast (71), the three-stage robust optimization part of the model must be solved first. To address the computational challenges, we design and implement the AOP-Looped C&CG Algorithm. The algorithm consists of two solving loops: the Outer-Loop C&CG and the Inner-Loop C&CG.

1) Outer-Loop C&CG

According to the (71), the Outer-Loop C&CG is implemented in a MP-SP scheme.

①The MP can be represented in (72).

$$\left\{\begin{array}{l}\underset{x\in X,w\in W}{min}A^Tx+\delta^TG+Fq+\eta\\ \quad\text{s.t.}a^Tx+b^Tw\leqslant C\\ \quad w^T+F+\delta k^T=0\\ \quad 0\leqslant G-k^Tq\leqslant\text{M}\nu\\ \quad 0\leqslant\delta\leqslant\text{M}(1-\nu)\\ c^Tx+d^Tv^{*,l}+e^Ty^l\leqslant D,\forall l\leqslant m\\ \quad f^Tx+g^Tv^{*,l}+h^Ty^l+\\ \quad i^Tu^{*,l}+j^Tz^l\leqslant E,\forall l\leqslant m\\ \quad \eta\geqslant v^Ty^l+B^Tz^l,\forall l\leqslant m\end{array}\right. \tag{72}$$

In (72), m represents the iteration index. η is an introduced auxiliary variable used to link MP and SP. $v^{*,l}$ and $u^{*,l}$ correspond to the worst-case scenarios of electricity price and source-load, respectively, obtained from SP in the l-th iteration. By solving MP and obtaining x^*, it can be substituted into SP.

②The SP can be represented in (73).

$$\left\{\begin{array}{l}\underset{v\in V}{max}\,\underset{y\in Y}{min}v^Ty+\underset{u\in U}{max}\underset{z\in Z}{min}B^Tz\\ \text{s.t.}c^Tx^*+d^Tv+e^Ty\leqslant D\\ \quad f^Tx^*+g^Tv+h^Ty+\\ \quad\quad i^Tu+j^Tz\leqslant E\end{array}\right. \tag{73}$$

2) Inner-Loop C&CG.

According to the (73), the Inner-Loop C&CG is implemented in a SPM-SPS scheme.

①The SPM can be represented in (74). The specific derivation process is shown in (A3)–(A6).

$$\begin{cases} \max\limits_{v\in V,y\in Y} \boldsymbol{\alpha}^T\left(\boldsymbol{c}^T\boldsymbol{x}^* + \boldsymbol{d}^T\boldsymbol{v} - \boldsymbol{D}\right) + \\ \sum\limits_{\tau}\left[(\boldsymbol{\beta}^\tau)^T\begin{pmatrix}\boldsymbol{f}^T\boldsymbol{x}^* + \boldsymbol{g}^T\boldsymbol{v} + \\ \boldsymbol{i}^T\boldsymbol{u}^{*,\tau} + \boldsymbol{j}^T\boldsymbol{z}^\tau - \boldsymbol{E}\end{pmatrix}\right] + \\ \sum\limits_{\tau}\left[(\boldsymbol{\gamma}^\tau)^T\left(\boldsymbol{B}^T\boldsymbol{z}^\tau\right)\right] \\ \text{s.t.}\boldsymbol{c}^T\boldsymbol{x}^* + \boldsymbol{d}^T\boldsymbol{v} + \boldsymbol{e}^T\boldsymbol{y} \leqslant \boldsymbol{D} \\ \boldsymbol{f}^T\boldsymbol{x}^* + \boldsymbol{g}^T\boldsymbol{v} + \boldsymbol{h}^T\boldsymbol{y} + \\ \boldsymbol{i}^T\boldsymbol{u}^{*,\tau} + \boldsymbol{j}^T\boldsymbol{z}^\tau \leqslant \boldsymbol{E}, \forall\tau\leqslant n \\ \varphi \geqslant \boldsymbol{B}^T\boldsymbol{z}^\tau, \forall\tau\leqslant n \\ \boldsymbol{\nu}^T + \boldsymbol{\alpha}\boldsymbol{e}^T + \boldsymbol{\beta}^\tau\boldsymbol{h}^T = 0, \forall\tau\leqslant n \\ 1 - \boldsymbol{\gamma}^\tau = 0, \forall\tau\leqslant n \\ 0 \leqslant \boldsymbol{D} - \left(\boldsymbol{c}^T\boldsymbol{x}^* + \boldsymbol{d}^T\boldsymbol{v} + \boldsymbol{e}^T\boldsymbol{y}\right) \leqslant \mathrm{M}\boldsymbol{\Lambda} \\ 0 \leqslant \boldsymbol{\alpha} \leqslant \mathrm{M}(1 - \boldsymbol{\Lambda}) \\ 0 \leqslant \boldsymbol{E} - \\ \begin{pmatrix}\boldsymbol{f}^T\boldsymbol{x}^* + \boldsymbol{g}^T\boldsymbol{v} + \\ \boldsymbol{h}^T\boldsymbol{y} + \boldsymbol{i}^T\boldsymbol{u}^{*,\tau} + \boldsymbol{j}^T\boldsymbol{z}^\tau\end{pmatrix} \leqslant \mathrm{M}\boldsymbol{\sigma}^\tau, \forall\tau\leqslant n \\ 0 \leqslant \boldsymbol{\beta}^\tau \leqslant \mathrm{M}(1 - \boldsymbol{\sigma}^\tau), \forall\tau\leqslant n \\ 0 \leqslant \varphi - \boldsymbol{B}^T\boldsymbol{z}^\tau \leqslant \mathrm{M}\boldsymbol{\omega}^\tau, \forall\tau\leqslant n \\ 0 \leqslant \boldsymbol{\gamma}^\tau \leqslant \mathrm{M}(1 - \boldsymbol{\omega}^\tau), \forall\tau\leqslant n \end{cases} \tag{74}$$

By solving SPM, values for $\boldsymbol{v}^*$ and $\boldsymbol{y}^*$ are obtained, which can then be substituted into SPS.

②SPS can be represented in (75). The specific derivation process is shown in (A7)–(A8).

$$\begin{cases} \max\limits_{u\in U,z\in Z} \boldsymbol{B}^T\boldsymbol{z} \\ \text{s.t}\boldsymbol{f}^T\boldsymbol{x}^* + \boldsymbol{g}^T\boldsymbol{v}^* + \boldsymbol{h}^T\boldsymbol{y}^* + \\ \boldsymbol{i}^T\boldsymbol{u} + \boldsymbol{j}^T\boldsymbol{z} \leqslant \boldsymbol{E} \\ \boldsymbol{B}^T + \boldsymbol{\xi}\boldsymbol{j}^T = 0 \\ 0 \leqslant \boldsymbol{E} - \\ \begin{pmatrix}\boldsymbol{f}^T\boldsymbol{x}^* + \boldsymbol{g}^T\boldsymbol{v}^* + \boldsymbol{h}^T\boldsymbol{y}^* + \\ \boldsymbol{i}^T\boldsymbol{u} + \boldsymbol{j}^T\boldsymbol{z}\end{pmatrix} \leqslant \mathrm{M}\boldsymbol{\theta} \\ 0 \leqslant \boldsymbol{\xi} \leqslant \mathrm{M}(1 - \boldsymbol{\theta}) \end{cases} \tag{75}$$

3) Pseudo-Code for AOP-Looped C&CG Algorithm.

The pseudo-code of the AOP-Looped C&CG Algorithm for the i-th IES is shown in Algorithm 1.

Algorithm 1: AOP-Looped C&CG Algorithm

Outer-Loop C&CG: Set $LB = -\infty$, $UB = +\infty$, $l = 0$, ε_1, $\boldsymbol{v}^{*,0}$, $\boldsymbol{u}^{*,0}$.

Repeat

Substitute $(\boldsymbol{v}^{*,l}, \boldsymbol{u}^{*,l})$ into MP, derive optimal $(\boldsymbol{x}^l, \boldsymbol{q}^l)$ and objective obj_{MP}^l, update $LB = \text{obj}_{\text{MP}}^l$.

Inner-Loop C&CG: Set $lb = -\infty$, $ub = +\infty$, $\tau = 0$, ε_2.

Repeat

Substitute $(\boldsymbol{x}^l, \boldsymbol{q}^l)$ into SPM, derive optimal $(\boldsymbol{v}^\tau, \boldsymbol{y}^\tau)$ and objective $\text{obj}_{\text{SPM}}^\tau$, update $lb = \text{obj}_{\text{SPM}}^\tau$.

Substitute $(\boldsymbol{x}^l, \boldsymbol{q}^l, \boldsymbol{v}^\tau, \boldsymbol{y}^\tau)$ into SPS, derive optimal $(\boldsymbol{u}^\tau, \boldsymbol{z}^\tau)$ and objective $\text{obj}_{\text{SPS}}^\tau$, update $ub = (\boldsymbol{v}^\tau)^T\boldsymbol{y}^\tau + \text{obj}_{\text{SPS}}^\tau$.

$\tau = \tau + 1$.

Until $|(ub - lb)/lb| < \varepsilon_2$, return $(\boldsymbol{v}^\tau, \boldsymbol{u}^\tau)$ as $(\boldsymbol{v}^{*,l}, \boldsymbol{u}^{*,l})$ to MP.

Update $ub = \boldsymbol{A}^T\boldsymbol{x}^l + (\boldsymbol{\delta}^l)^T\boldsymbol{G} + \boldsymbol{F}\boldsymbol{q}^l + \text{obj}_{\text{SPM}}^\tau$.

$l = l + 1$.

Until $|(UB - LB)/LB| < \varepsilon_1$, output optimal results.

5.4. ADMM algorithm

The ADMM algorithm demonstrates good convergence properties for large-scale variable optimization problems, while also ensuring the privacy of information during cooperative operation among entities. Therefore, we employ the ADMM algorithm to sequentially solve P1: (71) and P2: (12).

1) P1:Cooperative benefit maximization subproblem.

To thoroughly solve (71), the AOP-Looped C&CG Algorithm is employed, which solves the three-stage robust optimization. Subsequently, the ADMM algorithm is utilized to solve the interaction power among the three IESs.

The pseudo-code for ADMM in P1 of the i-th IES is shown in algorithm 2.

Algorithm 2: ADMM for subproblem 1

Set $\mathrm{iter}_1 = 1, \varepsilon_3, \rho_{ij,1}, \boldsymbol{\lambda}_{ij,1}, (j \in J, j \neq i)$

Repeat

Solving the i-th IES model to get $P_{ij,t}^{e,\mathrm{iter}_1}$.

Update $\lambda_{ij,1,t}^{\mathrm{iter}_1} = \lambda_{ij,1,t}^{\mathrm{iter}_1} + \rho_{ij,1}\left(P_{ij,t}^{e,\mathrm{iter}_1+1} + P_{ji,t}^{e,\mathrm{iter}_1+1}\right)$.

Calculate $\mathrm{toler}_1^{\mathrm{iter}_1} = \sum_t \sum_{j\in J, j\neq i} \left\| P_{ij,t}^{e,\mathrm{iter}_1+1} + P_{ji,t}^{e,\mathrm{iter}_1+1} \right\|_2^2$.

$\mathrm{iter}_1 = \mathrm{iter}_1 + 1$.

Until $\mathrm{toler}_1^{\mathrm{iter}_1} < \varepsilon_3$, output optimal results.

2) P2:Energy transaction payment subproblem.

By solving P1 to obtain $P_{ij,t}^{e}$ and C_i^*, and substituting C_i^0 obtained by setting the transaction volume to 0 into P2, the ADMM algorithm is then employed to solve the interaction electricity prices among the three IESs.

The pseudo-code for ADMM in P2 of the i-th IES is shown in algorithm 3.

Algorithm 3: ADMM for subproblem 2

Set $\mathrm{iter}_2 = 1, \varepsilon_4, \rho_{ij,2}, \boldsymbol{\lambda}_{ij,2}, (j \in J, j \neq i)$

Repeat

Solving the i-th IES model to get $p_{ij,t}^{e,\mathrm{iter}_2}$.

Update $\lambda_{ij,2,t}^{\mathrm{iter}_2} = \lambda_{ij,2,t}^{\mathrm{iter}_2} + \rho_{ij,2}\left(p_{ij,t}^{e,\mathrm{iter}_2+1} - p_{ji,t}^{e,\mathrm{iter}_2+1}\right)$.

Calculate $\mathrm{toler}_2^{\mathrm{iter}_2} = \sum_t \sum_{j\in J, j\neq i} \left\| p_{ij,t}^{e,\mathrm{iter}_2+1} - p_{ji,t}^{e,\mathrm{iter}_2+1} \right\|_2^2$.

$\mathrm{iter}_2 = \mathrm{iter}_2 + 1$.

Until $\mathrm{toler}_2^{\mathrm{iter}_2} < \varepsilon_4$, output optimal results.

5.5. ADMM algorithm coupled with AOP-looped C&CG

The P1 we consider is a three-level Nash three-stage robust optimization model. Therefore, we propose a coupled AOP-Looped C&CG ADMM algorithm to fully solve P1. The flowchart of this algorithm is depicted in Fig. 7.

Remark 5. The solution algorithm (ADMM) for the P2 problem we consider follows a similar flowchart as shown in Fig. 7. Here, we will not delve into the details.

6. Case studies

6.1. Basic data and system structure description

In this study, a simulation analysis is conducted using three interconnected IESs as an example. There are differences among the IESs, with PV prosumers present in IES1 and IES3, while IES2 consists solely

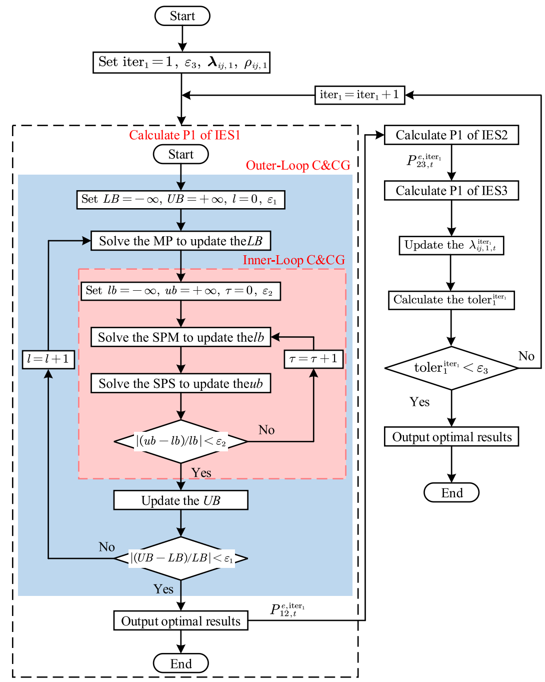

Fig. 7. ADMM algorithm flow chart coupled with AOP-Looped C&CG.

of common users.

The predicted electricity price for purchasing and selling electricity from the external grid, as well as the gas purchase price from the natural gas company, are shown in Table A1. The parameters for energy conversion devices, storage devices, efficiency, and operating limits are presented in Table A2. The algorithm parameters are outlined in Table A3. The operating and algorithm parameters are consistent across all IESs. The load and renewable energy output prediction curves for each IES, as well as the load and photovoltaic output prediction curves for PV prosumers or load prediction curves for common users, are illustrated in Fig. A1-Fig. A3. Electricity prices and source-load are considered as uncertain factors in the system, with uncertainty sets defined by 10%, 15%, and 10% fluctuations from their predicted value [22].

The scheduling period in this study is set to 1 day, with a time interval of 1 h for scheduling. All simulation examples are performed on a microcomputer equipped with an 8-core 2.30GHZ processor and 8GB of memory. The programming platform used is MATLAB2020b, and the YALMIP toolbox is employed for model formulation. The GUROBI and MOSEK commercial solvers are utilized for solving.

6.2. Scheduling plan

6.2.1. Convergence analysis

The convergence curves of operational cost and residual error for each IES and the IES alliance are obtained by solving P1 using the ADMM algorithm coupled with AOP-Looped C&CG, as depicted in Fig. 8. It can be observed that the residual of transactional power reaches the convergence criterion at the 46th iteration, indicating excellent convergence performance of the algorithm. Through local communication and collaborative optimization, the operational cost of each IES converge to the optimal values of 17,082.74 ¥, 17,287.20 ¥, and 23,623.73 ¥, respectively. The corresponding operational cost of the IES alliance gradually converge to the optimal value of 57,993.67 ¥. Moreover, the adopted distributed optimization method only requires the exchange of expected interactive power information, eliminating the need for global communication and effectively preserving the privacy of all participating entities. The modeling algorithm solution time is

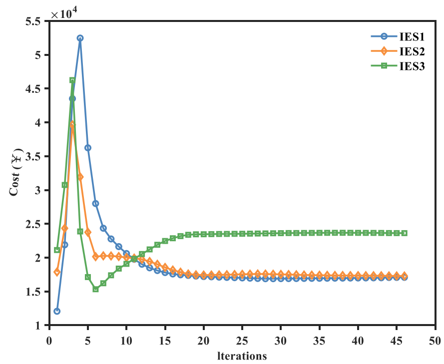

(a) Operating cost of each IES

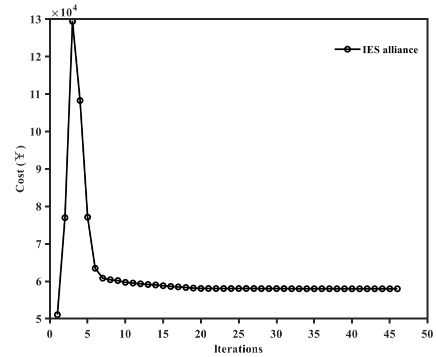

(b) IES alliance operating cost

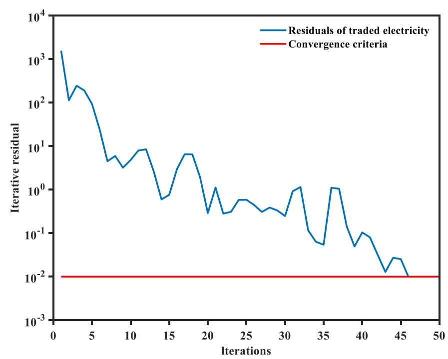

(c) Residual

Fig. 8. P1 distributed iterative convergence of IES.

4167.9 s.

By employing the ADMM algorithm to solve P2, the convergence curves of transaction cost and residual error for each IES and the IES alliance are obtained, as shown in Fig. 9. Due to the small scale of the problem, the residual of transactional electricity price reaches the convergence criterion after 16 iterations. The transaction cost of each IES converge to the optimal value of −504.07￥, 3436.13￥, and −2931.52￥, respectively. Throughout the iteration process, their transaction cost exhibit some fluctuations, reflecting the bargaining process among the three IESs. The corresponding transaction cost of the IES alliance converge to the optimal value of 0.54￥, which is close to 0 and signifies the internal balance of energy trading. The modeling algorithm solution time is 20.2 s.

Remark 6. The cooperative game Nash bargaining model between PV prosumers within IES1 and IES3 does not require the utilization of the ADMM algorithm for solving since P1 employs a centralized optimization strategy. However, for P2, which adopts a distributed optimization strategy, the use of the ADMM algorithm is still necessary. The convergence curves for these models are illustrated in Fig. B1-Fig. B2.

To analyze the performance of the AOP-Looped C&CG algorithm, the convergence processes of each IES at the 1st and 46th iteration under the distributed overall problem-solving framework are demonstrated, as shown in Fig. 10-Fig. 11. The upper and lower bound of the outer problem objective for each IES continuously approach each other, satisfying the convergence criterion by the second iteration. The inner problem requires two iterations to converge during the first outer iteration, while in the second outer iteration, it directly identifies the worst-case scenario and achieves convergence. Numerically, the decrease in outer cost is attributed to the strong purchasing behavior of the PV prosumer or common user in the lower level, generating significant profit that offset the upper-level IES. The three-stage robust optimization model for each IES are highly complex and challenging to solve using conventional method. However, the selected solution approach exhibits excellent convergence performance.

6.2.2. Interactive power analysis

1) The interaction power between IESs

The energy exchange among IESs is crucial for enhancing the overall system efficiency, as it no longer relies solely on their individual supply capabilities. In an energy-deficient system, energy can be purchased from energy-abundant systems. The scheduling results of electricity exchange among IESs are illustrated in Fig. 12. Influenced by factors such as load level, energy price, and multi-energy matching degree, IES2 primarily purchases electricity from other IESs. During the period of 9:00–15:00, when the electricity load level of IES1 and IES3 are relatively low, and there is abundant photovoltaic generation, surplus electricity is transmitted to IES2, which has lower wind power output and higher load. During the off-peak period with lower electricity price at night, the wind power output of IES2 relatively increases, enabling it to supply electricity to other IESs. It is worth noting that the overall electricity exchange among IESs sums up to 0 during different time intervals, satisfying the internal balance constraint of the exchange power.

2) The interaction power between PV prosumers

Within each IES, there also exist electricity exchange among PV prosumers to achieve cooperation and mutual benefit among lower-level

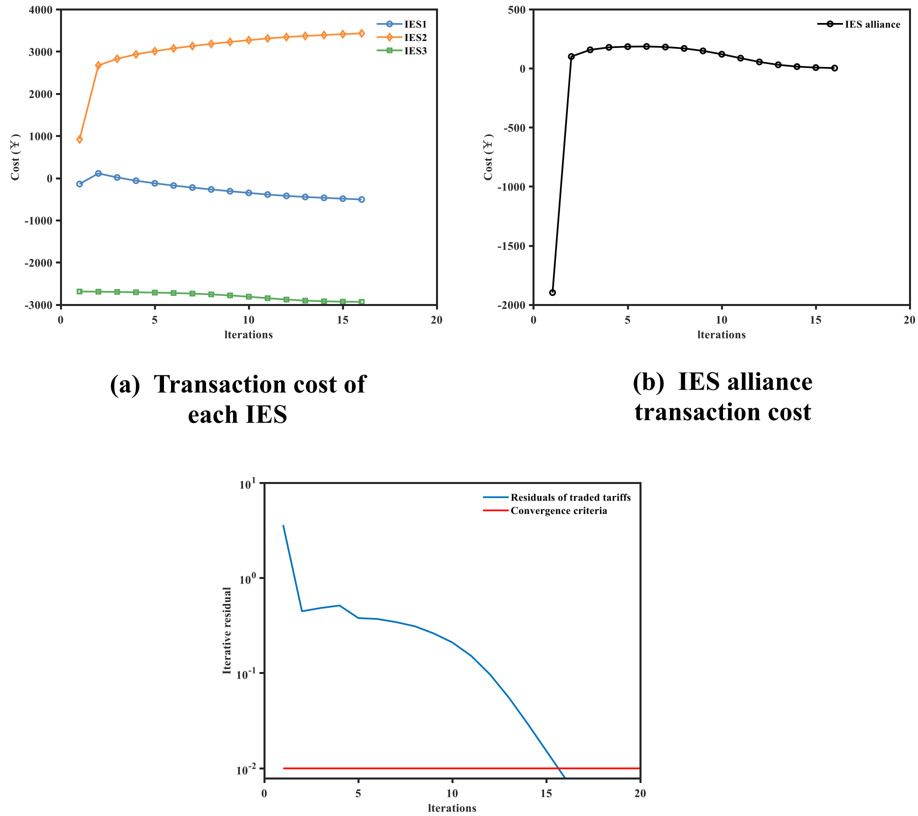

(a) Transaction cost of each IES

(b) IES alliance transaction cost

(c) Residual

Fig. 9. P2 distributed iterative convergence of IES.

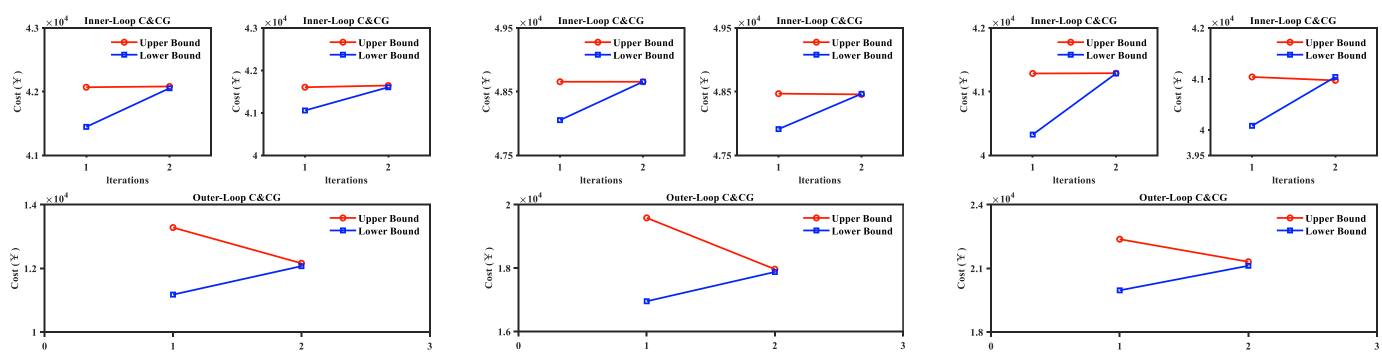

(a) IES1

(b) IES2

(c) IES3

Fig. 10. 1st Iteration.

users, as shown in Fig. 13. In IES1, PV prosumers frequently engage in electricity exchange during different time intervals based on their energy supply-demand matching degree, further reducing their individual energy consumption levels. In IES3, PV prosumer3 has a higher proportion of photovoltaic generation, and PV prosumer2 exhibits significant differences in load conditions compared to other PV prosumers. As a result, the energy exchange among PV prosumers becomes more pronounced. PV prosumer1 sells electricity during periods of lower photovoltaic generation and purchases electricity during periods of higher photovoltaic generation, while PV prosumer3 exhibits the opposite pattern. PV prosumer2, on the other hand, predominantly purchases electricity throughout most time intervals.

6.2.3. *Worst-case scenario analysis*

The worst-case scenario of IES1 obtained through the three-stage robust optimization model are shown in Fig. 14, while those of IES2 and IES3 are depicted in Fig. B3-Fig. B4. Taking IES1 as an example for analysis, it can be observed that the obtained worst-case scenario mostly exhibit increased electricity purchase price, decreased electricity selling price, increased generation cost, and decreased load shedding. These results align with the optimal requirement of the robust model for operating cost under worst-case scenario. Regarding the obtained worst-case electricity price scenario, the uncertainty in purchase and selling price mainly occur during the periods of 12:00–14:00 and 19:00–22:00, which are peak electricity price periods associated with larger price fluctuations and higher cost increments. It is worth noting that within the obtained worst-case scenario, there are a few points that contradict

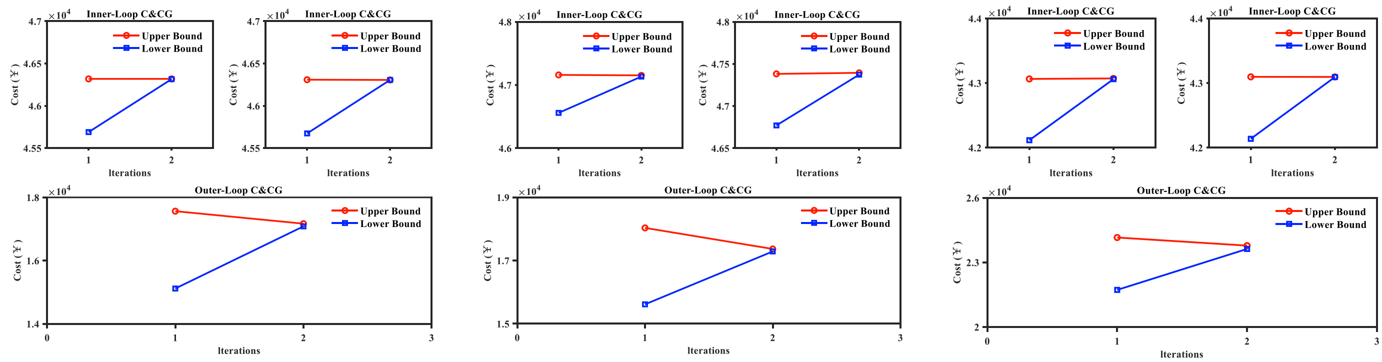

(a) IES1 (b) IES2 (c) IES3

Fig. 11. 46th iteration.

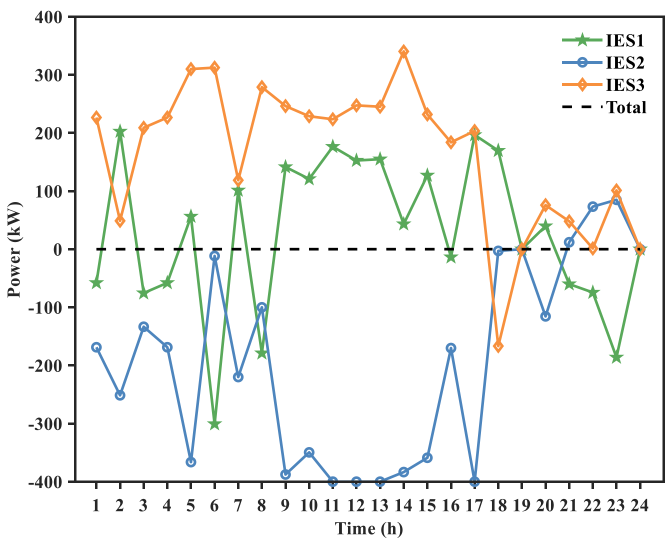

Fig. 12. Energy trading results between IESs.

the selected upper and lower bounds. This is due to frequent switching of the state of EES, EHM, and electricity purchase and selling, resulting in increased scheduling and operational cost for the system, leading to a higher overall cost value.

6.2.4. Schedule plan analysis

The scheduling and operational plans for IES1 are shown in Fig. 15, while those for IES2 and IES3 are displayed in Fig. B5-Fig. B6. Taking IES1 as an example, we will analyze its electricity, heat, and the scheduling plans for internal PV prosumers. IES1 can achieve a supply-demand balance for both electricity and heat at any given time interval within the scheduling period. Regarding the electricity scheduling plan, the internal photovoltaic generation within the system is given the highest priority in the energy dispatch, ensuring its full utilization. The system meets the electricity demand through various means, including electricity exchange, electricity generation by GHDCHP, electricity discharge from EES, electricity generation by EHM, and purchasing electricity from the external grid. During the period of 1:00–7:00, when electricity prices are relatively low, the system purchases a significant amount of electricity from the grid. The shortfall is primarily compensated by electricity generation from GHDCHP and electricity purchase through exchange. Considering the system's optimization throughout the entire time period, the EES is charged during this period. From 8:00–11:00 and 15:00–18:00, when electricity prices are normal, the electricity demand of the system is met through a combination of GHDCHP and external electricity purchase, with EHM also operating and selling a portion of the electricity. From 17:00–18:00, as the electricity demand increases, EHM operates to meet the energy supply

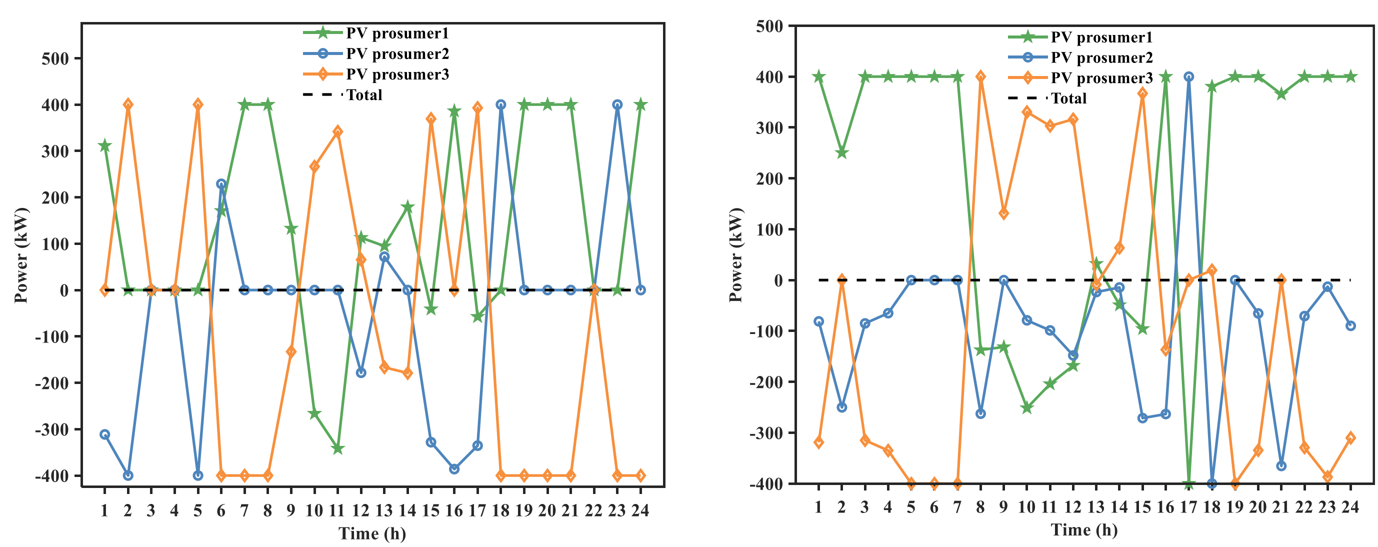

(a) PV prosumer of IES1 (b) PV prosumer of IES3

Fig. 13. Energy trading results between PV prosumers.

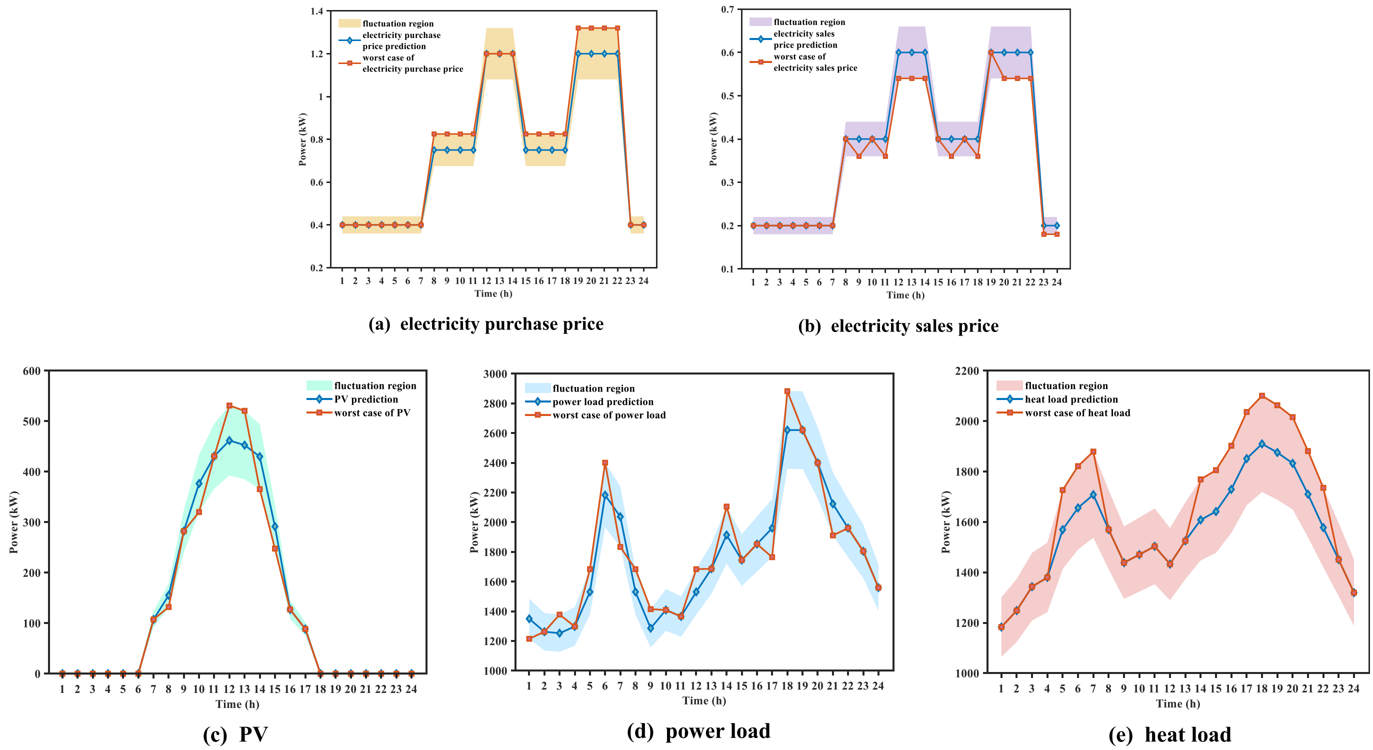

(a) electricity purchase price (b) electricity sales price

(c) PV (d) power load (e) heat load

Fig. 14. Worst case of IES1.

requirements. During 12:00–14:00 and 19:00–22:00, when electricity prices are at peak levels, the system relies mainly on GHDCHP for energy supply, with supplemental electricity purchases from the external grid. EHM and EES discharge a substantial amount of electricity to meet the demand. From 23:00–24:00, when electricity prices are low, the system first purchases electricity from the external grid, and any shortfall is supplemented by electricity generation from GHDCHP. The heat supply within the system is relatively straightforward, with heat generation from GHDCHP and a small amount from GB sufficient to meet the heat demand of the system and PV prosumers.

Within IES1, each PV prosumer in the lower level participates in demand response activities, reducing their energy demands to lower energy costs and improve energy utilization efficiency. Each PV prosumer satisfies their electricity demand through rooftop photovoltaic installations and electricity purchases from IES1, while their heat demand is met by purchasing heat from IES1. There are significant variations in the matching between the photovoltaic generation and energy consumption of each PV prosumer. Therefore, they further enhance their electricity usage efficiency through electricity exchange among themselves.

By analyzing the scheduling and operational plans of IES1, the interdependency and coordination among different energy supply components are observed, working together to meet the load demands. Similar analyses can be applied to the scheduling and operational plans of other IESs and the energy consumption patterns of lower-level users. However, we will not repeat these analyses here.

6.3. Trading pricing strategy

The transaction electricity prices between IESs are obtained through the solution of P2, as shown in Fig. 16. The transaction prices for each time interval fall within the range of electricity purchase and sale price from the external grid, effectively preventing any arbitrage activities between IESs. Consequently, when an IES experiences an energy shortage, it prioritizes transactions with IESs that offer lower energy price and have sufficient energy supply. In turn, the selling IES can gain certain profits from these transactions, thereby reducing the overall operating cost.

Further analysis is conducted on the energy transaction prices within each IES. The transaction prices for electricity and heat between IES1 and its three internal PV prosumers are shown in Fig. 17, while those for IES2 and IES3 are displayed in Fig. B7-Fig. B8. In the case of IES1, the internal selling prices set by IES1 for the three PV prosumers are identical and fall within the range of electricity purchase and sale prices from the external grid. The internal heat prices are also determined within certain limits. These energy prices are established to satisfy the interests and demands of both IES1 as the upper-level entity and the PV prosumers as the lower-level entities.

Meanwhile, energy sharing transactions between the PV prosumers within IES1 and IES3 are conducted based on Nash bargaining strategy, and the resulting transaction electricity prices among the PV prosumers are shown in Fig. 18 and Fig. B9. Taking the transaction electricity prices among the PV prosumers within IES1 as an example for analysis, these prices are lower than the prices for purchasing electricity from the upper-level IES1. Furthermore, pricing for each time interval is determined based on the energy consumption patterns of each PV prosumer, facilitating cooperation and mutual benefit among the PV prosumers.

6.4. Comparison of scheduling plans

6.4.1. Comparative analysis of IES interconnection and independent operation

In energy dispatch, the EHM plays a significant role in smoothing the volatility of renewable energy. Its effectiveness is further highlighted when MIES operate in an interconnected manner, leading to improved overall energy efficiency. When IESs are interconnected or operate independently, the EHM dispatch plans for IES1 are shown in Fig. 19, while those for IES2 and IES3 are displayed in Fig. B10-Fig. B11. Taking IES1 as an example, we analyze the situations of EHM in the P2H and H2P states during interconnected and independent operations. During interconnected operation, P2H is concentrated during off-peak electricity prices or when there is higher renewable energy generation, while

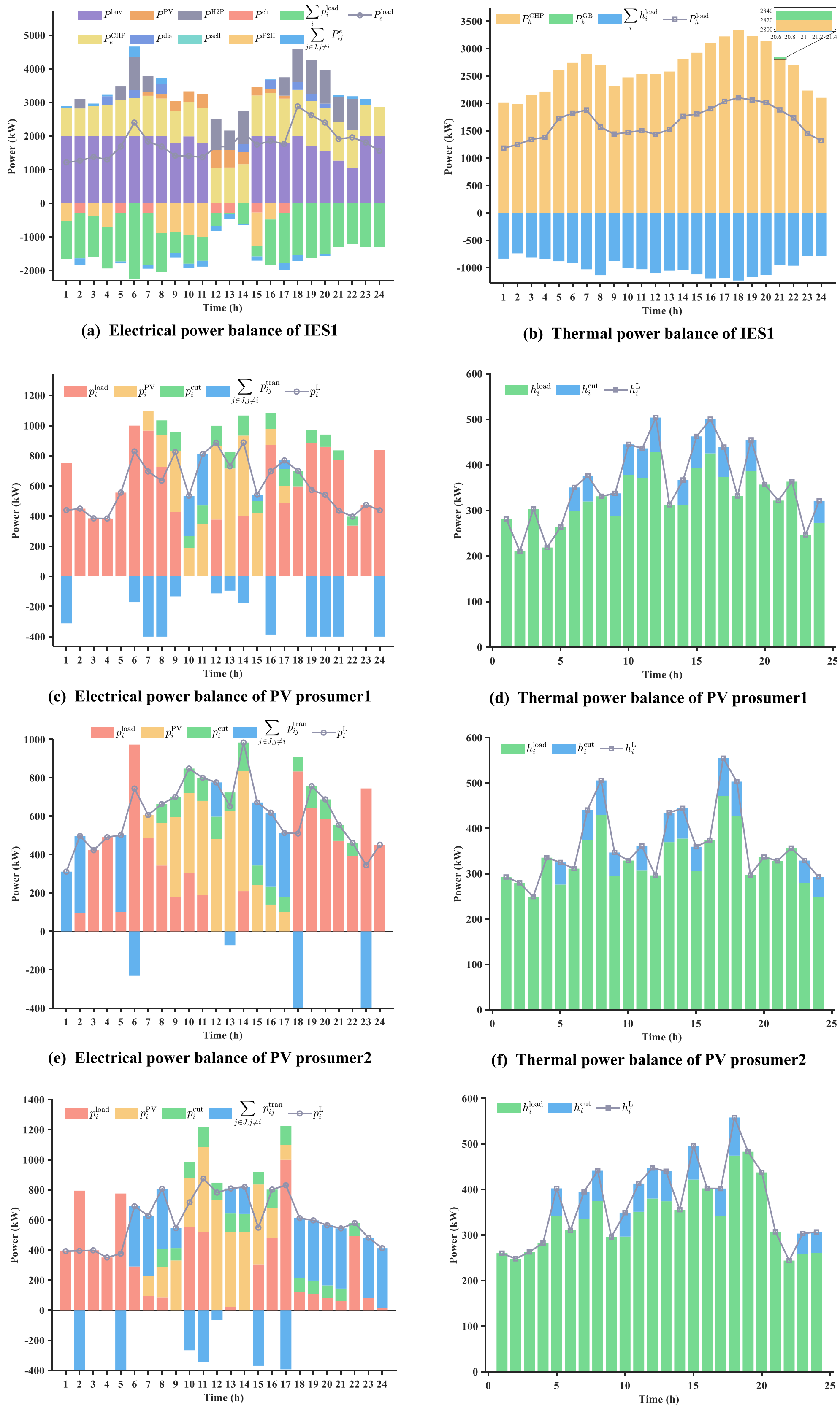

(a) Electrical power balance of IES1

(b) Thermal power balance of IES1

(c) Electrical power balance of PV prosumer1

(d) Thermal power balance of PV prosumer1

(e) Electrical power balance of PV prosumer2

(f) Thermal power balance of PV prosumer2

(g) Electrical power balance of PV prosumer3

(h) Thermal power balance of PV prosumer3

Fig. 15. Energy balance of IES1.

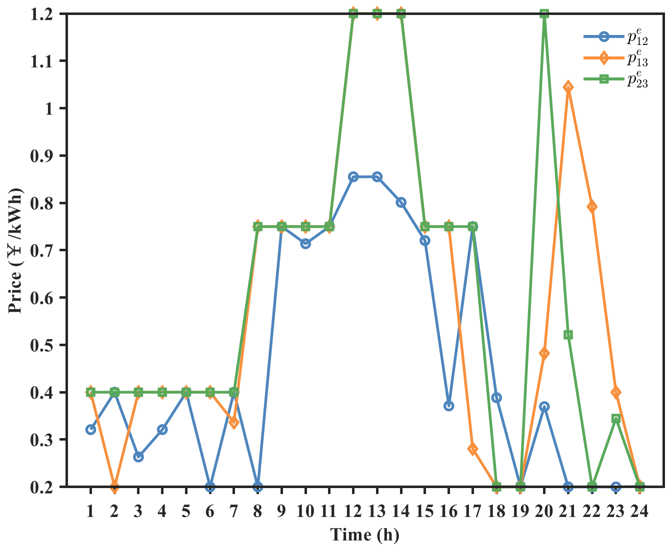

Fig. 16. Transaction electricity price results between IES.

H2P is concentrated during peak electricity prices and when renewable energy generation is lower. This allows for effective utilization of clean renewable energy generation. Compared to independent operation, both P2H and H2P energy quantities are smaller during interconnected operation, as the system prioritizes energy exchange to meet overall demand and utilizes energy storage devices to further enhance energy efficiency within the IES.

By solving P1 and P2 through distributed sequential computations, the final costs of each IES under interconnected operation are determined. Table 2 presents the cost comparisons before and after transaction settlement for each IES. Additionally, the cost comparisons before and after transaction settlement for the PV prosumers within IES1 and IES3 are shown in Table B1-Table B2. Taking the cost comparisons before and after transaction settlement for each IES as an example, it can be observed that the overall costs of interconnected operation consist of the costs before transactions and the transaction costs. Through calculations, it is found that the costs of independent operation, where there is no energy exchange among IESs, are higher than the overall costs of interconnected operation. These reductions in costs are 4.59%, 24.81%, and 1.29% for each IES, respectively, satisfying the cooperative premise of Nash bargaining. Moreover, the final costs of the IES alliance under interconnected operation are significantly lower compared to independent operation, with a reduction ratio of 10.63%. This demonstrates the effectiveness of the proposed method in balancing both the overall economic benefits and the individual interests of IESs.

6.4.2. *Comparative analysis of uncertain scenarios and deterministic scenarios*

A comparison is made between the scheduling operation plan state variables in Section 6.2.4 and the deterministic scenario. The comparison of scheduling operation plan state variables for IES1 is shown in Fig. 20, while those for IES2 and IES3 are displayed in Fig. B12-Fig. B13. Taking IES1 as an example, an analysis is conducted. The electricity mismatch caused by source-load fluctuations can be mitigated through the utilization of EHM, EES, and direct electricity purchase and sale. Compared to the deterministic scenario, the differences in time-based electricity purchase and sale prices are significant, resulting in similar electricity purchase and sale states. The EHM operates in the P2H state to produce hydrogen from 3:00 to 4:00, ceases hydrogen production during the midday period due to insufficient photovoltaic hydrogen production capacity, and terminates hydrogen production early at 17:00. On the other hand, the EES experiences fluctuations mainly during periods of high electricity prices. Through optimization of the scheduling operation plan state variables, the conservatism of the energy dispatch plan is further improved.

A comparison is made between Section 6.2.4 and the deterministic scenario in terms of external energy port power variations, aiming to analyze the impact of multiple uncertainties in electricity prices and source-load fluctuations on system operation. The external energy port power variations for IES1 are shown in Fig. 21, while those for IES2 and IES3 are displayed in Fig. B14-Fig. B15. Taking IES1 as an example, an analysis is conducted. The robust uncertainties in electricity prices and source-load fluctuations allow the system to rely on external energy purchases to meet its reserve requirements. However, due to considering the worst-case scenario, the system no longer sells electricity to the external grid but adjusts its electricity purchases based on the worst-case scenario obtained. Overall, the system's electricity purchases and gas purchases are increased compared to the deterministic scenario.

6.5. *Model advantage comparison and sensitivity analysis*

The proposed method is compared with a deterministic optimization model, a static robust optimization model, and a two-stage robust

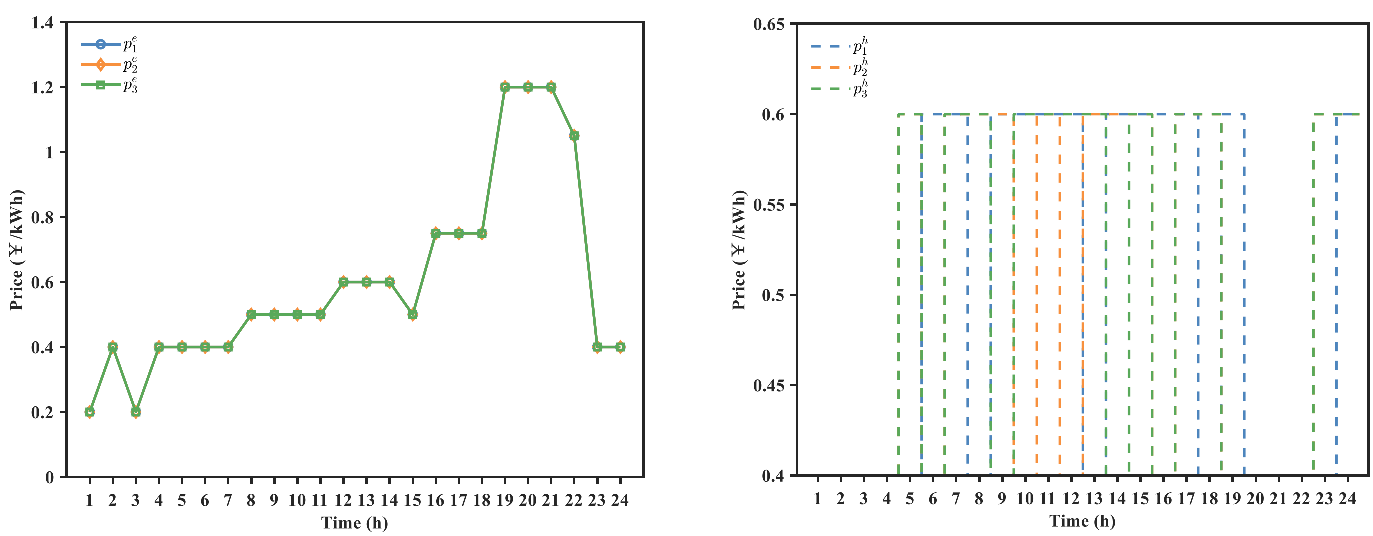

(a) electricity price **(b) heat price**

Fig. 17. IES1 Stackelberg game energy transaction price.

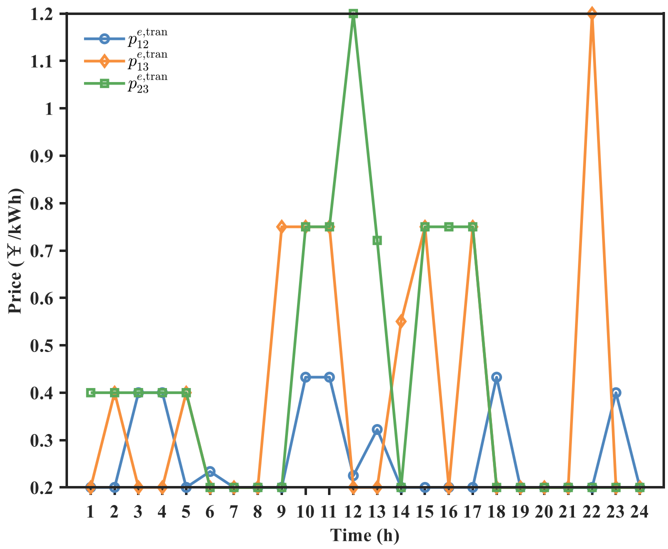

Fig. 18. Transaction electricity price results between PV prosumers within IES1.

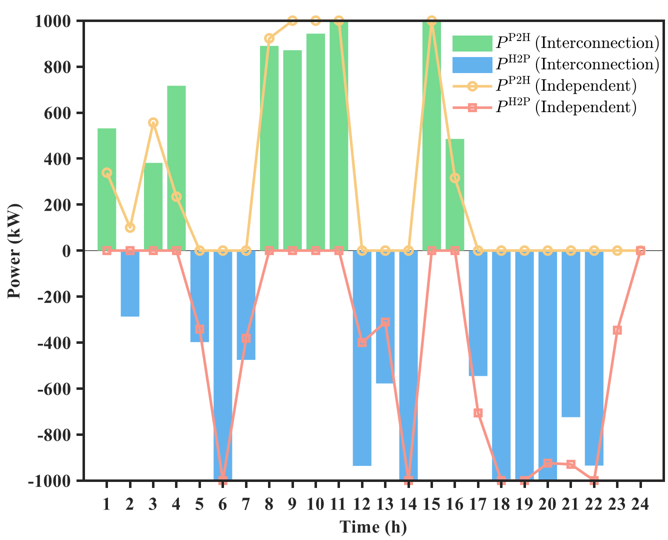

Fig. 19. EHM scheduling plan for IES1.

Table 2
Pre- and post-trade settlement costs for each IES.

Cost	IES1	IES2	IES3	IES alliance
Independent operation cost/$	17,338.84	25,864.67	20,958.29	64,161.80
Interconnection operation without transaction cost/$	17,082.74	17,287.20	23,623.72	57,993.67
Transaction cost/$	−504.07	3436.13	−2931.52	0.54
Final cost of interconnection operation/$	16,578.67	20,723.33	20,692.20	57,994.20
Cost reduction value/$	760.17	5141.34	266.09	6167.60

optimization model that only considers source-load uncertainties. The results are shown in Table 3. It can be observed that compared to the deterministic optimization model, the model proposed in this paper takes into account the multiple uncertainties in electricity prices and source-load fluctuations. Although the operating costs are higher, the system's loss of load is significantly reduced, better meeting the system's energy supply demands. Compared to the static robust optimization model, the proposed model shows significant improvement in conservatism. Compared to the two-stage robust optimization model, the operating costs are increased in the proposed model. This is because the proposed model also incorporates the uncertainties in electricity prices into the operating costs, which cannot be ignored in practical operation. The loss of load [25] is an evaluation metric used to represent the system risk.

The sensitivity analysis of system uncertainties is conducted using a multi-run simulation approach. The uncertain variables are randomly assigned a number of time periods equal to their uncertainty value and are sampled randomly within their respective sets. This process is repeated 500 times to generate practical scenarios for electricity prices and source-load. The uncertainty level is uniformly represented by the uncertainty ratio, which ranges from 0 to 1 with a step size of 1/6, indicating the proportion of uncertain time periods to the total time periods. The corresponding total operating costs and loss of load variations are shown in Table 4. It can be observed that the operating costs are positively correlated with the uncertainty ratio, while the loss of load is negatively correlated. This reflects the influence of uncertain parameters on robust scheduling plans. When the uncertainty ratio is 0, corresponding to the deterministic optimization results, the system achieves the lowest costs but experiences the highest loss of load. This high return is accompanied by high risk. As the uncertainty ratio increases, the costs continue to rise due to the consideration of more uncertain time periods. However, the system's reserve capacity increases, leading to a gradual reduction in the loss of load and an enhancement in the reliability of energy supply. When the uncertainty ratio is 1, representing the consideration of uncertainty in all time periods, the loss of load is smaller, but the operating costs are higher. Achieving low risk requires a significant investment. Reasonable uncertainty parameters are essential to meet the load requirements in uncertain time periods effectively.

Upon comprehensive comparison, this paper takes into account the multiple uncertainties in electricity prices and source-load, which provides advantages in terms of both economic performance and robustness. Additionally, the adjustments are more flexible. It is worth noting that the uncertainty-related parameters in the case study are analyzed from an overall perspective, and the parameters are consistent across all IESs. In practical implementation of scheduling strategies, each IES can adjust its operational strategies flexibly by selecting appropriate uncertainty parameters based on its own circumstances, thus achieving a balance between returns and risks.

7. Conclusion

This paper focuses on the MIES distributed P2P electricity trading considering the multiple uncertainties in electricity prices and source-load, incorporating EHM and GHDCHP. A three-level Nash three-stage robust optimization model is proposed to capture the coupling relationship between the game and robustness. Finally, an ADMM algorithm, coupling AOP-Looped C&CG, is proposed to solve the proposed model in a distributed manner. The main conclusions are as follows:

1) The proposed IES, which integrates EHM and GHDCHP to couple multiple energy flows, serves to mitigate the volatility of renewable energy and improve the overall energy efficiency of the system.
2) The proposed Nash-Stackelberg-Nash game framework in this paper serves two purposes. On one hand, the individual characteristics between IESs and users can be effectively described through the master-slave game, allowing the decoupling of interests between sources and loads. IESs can guide users to respond to demand by setting energy prices. On the other hand, the Nash game between IESs and PV prosumers enhances the economic benefits of the IES

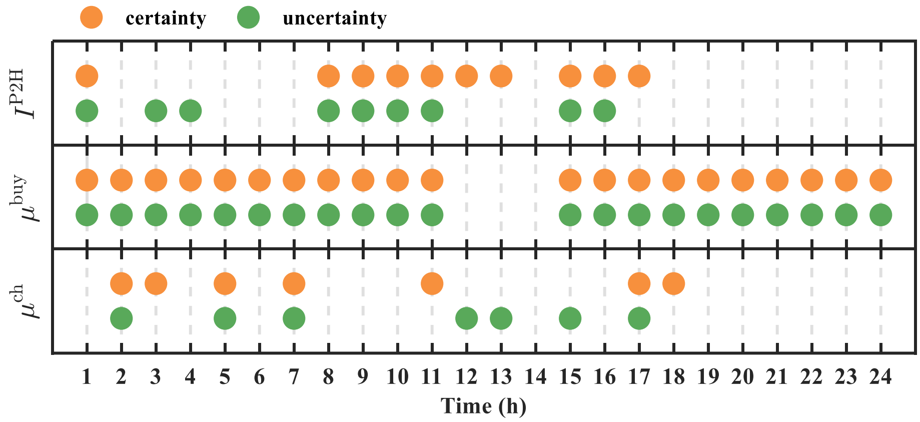

Fig. 20. Comparison of state variables of IES1 scheduling operation plan.

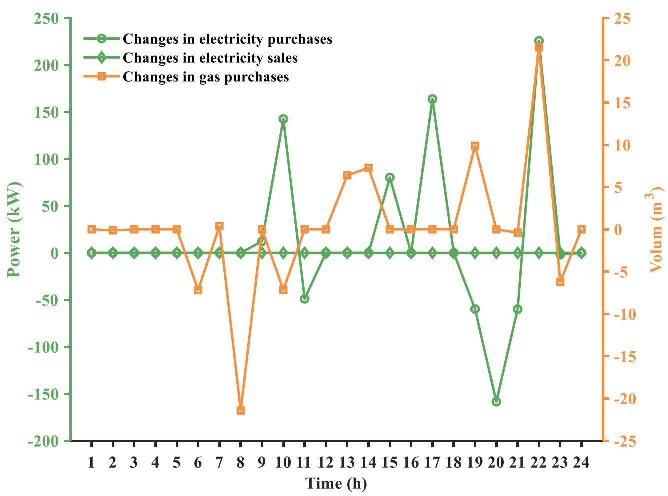

Fig. 21. Changes in the power of the external energy port of IES1.

Table 3
Comparison of model advantages.

model	operation cost/￥	load shedding/kW
this article	57,993.67	1600.51
certainty	51,290.33	3832.66
static robust	59,774.21	1502.43
two-stage robust	55,239.38	189.72

Table 4
Sensitivity analysis.

proportion of uncertainty	operation cost/￥	load shedding/kW
0	51,290.33	3832.66
1/6	54,188.85	2760.19
2/6	56,011.56	2008.10
3/6	57,993.67	1600.51
4/6	59,142.97	487.60
5/6	59,963.28	38.76
1	60,423.00	0

alliance and PV prosumer alliance, while ensuring fairness in the interests between IESs and PV prosumers.

3) The proposed three-level Nash three-stage robust optimization model in this paper can effectively address the risks brought by the multiple uncertainties in electricity prices and source-load, achieving a balance between the economic performance and conservatism of multiple IESs. Additionally, the distributed solution of this model using the proposed ADMM algorithm, coupling AOP-Looped C&CG, exhibits excellent convergence performance.
4) Considering the multiple uncertainties in electricity prices and source-load, the robust scheduling plan of the system experiences an increase in operational costs and an improved ability to cope with risks. The conservatism of the plan is dependent on the values of uncertain parameter sets. In practice, each IES can flexibly adjust its operational strategy by selecting appropriate uncertain parameters based on its individual circumstances, achieving a balance between benefits and risks.

In the next step, the actual distribution characteristics of electricity prices and source-load will be investigated to reduce the conservatism of robust optimization by considering the uncertainty set of multiple interval electricity prices and source-load. Due to the integration of multiple heterogeneous energy sources (electricity, heat, gas, and hydrogen) within the Integrated Energy System (IES), the power distribution network not only includes an electrical grid and a heat network but also incorporates natural gas pipelines and hydrogen pipelines. Consequently, the external energy grid, along with internal energy conversion devices, provides energy to meet the load requirements and ensures the supply-demand balance.

CRediT authorship contribution statement

Zongnan Zhang: Writing – review & editing, Writing – original draft, Visualization, Validation, Software, Resources, Project administration, Methodology, Investigation, Funding acquisition, Data curation. **Kudashev Sergey Fedorovich:** Supervision, Formal analysis, Conceptualization.

Declaration of competing interest

The authors declare that they have no competing interests.

Data availability

No data was used for the research described in the article.

Appendix A. Appendix

(1) A Nash bargaining model is proposed for cooperative game among PV prosumer aggregator members.

For the subproblem P1 of maximizing cooperation benefit, the decision model for the *i*-th PV prosumer can be formulated as (A1).

$$\begin{cases} \min\limits_{q \in Q} \left(C^{\mathrm{tran}} + C^{\mathrm{dr}} \right) \\ \text{s.t.}(47)、(54) - (59) \end{cases} \tag{A1}$$

The decision model for the *i*-th PV prosumer can be formulated as (A2) for the subproblem P2 of energy transaction payment.

$$\begin{cases} \min \begin{Bmatrix} -\ln\left(U_i^0 - U_i^* + \sum\limits_t \sum\limits_{j \in J, j \neq i} p_{ij,t}^{e,\mathrm{tran}} p_{ij,t}^{\mathrm{tran}} \right) + \\ \sum\limits_t \sum\limits_{j \in J, j \neq i} \begin{bmatrix} \lambda_{ij,3,t} \left(p_{ij,t}^{e,\mathrm{tran}} - p_{ji,t}^{e,\mathrm{tran}} \right) + \\ \frac{\rho_{ij,3}}{2} \left\| p_{ij,t}^{e,\mathrm{tran}} - p_{ji,t}^{e,\mathrm{tran}} \right\|_2^2 \end{bmatrix} \end{Bmatrix} \\ \text{s.t.} U_i^0 - U_i^* + \sum\limits_t \sum\limits_{j \in J, j \neq i} p_{ij,t}^{e,\mathrm{tran}} p_{ij,t}^{\mathrm{tran}} \geqslant 0 \\ (49) \end{cases} \tag{A2}$$

In (A2), $\lambda_{ij,3,t}$ is the Lagrange multiplier, $\rho_{ij,3}$ is the penalty factor, U_i^0 represents the cost for the *i*-th PV prosumer when not participating in energy transactions, which can be obtained by setting the transaction volume to 0, and U_i^* represents the optimal cost obtained by solving the subproblem of maximizing cooperative benefits for the *i*-th PV prosumer.

(2) Derivation of SPM

$$\begin{cases} \max\limits_{\boldsymbol{v} \in V} \min\limits_{\boldsymbol{y} \in Y} \boldsymbol{v}^T \boldsymbol{y} + \varphi \\ \text{s.t.} \boldsymbol{c}^T \boldsymbol{x}^* + \boldsymbol{d}^T \boldsymbol{v} + \boldsymbol{e}^T \boldsymbol{y} \leqslant \boldsymbol{D} : \boldsymbol{\alpha} \\ \boldsymbol{f}^T \boldsymbol{x}^* + \boldsymbol{g}^T \boldsymbol{v} + \boldsymbol{h}^T \boldsymbol{y} + \\ \boldsymbol{i}^T \boldsymbol{u}^{*,\tau} + \boldsymbol{j}^T \boldsymbol{z}^\tau \leqslant \boldsymbol{E} : \boldsymbol{\beta}^\tau, \forall \tau \leqslant n \\ \varphi \geqslant \boldsymbol{B}^T \boldsymbol{z}^\tau : \boldsymbol{\gamma}^\tau, \forall \tau \leqslant n \end{cases} \tag{A3}$$

Since (A3) is a bi-level optimization problem, it is necessary to convert the lower-level model into upper-level constraints using the KKT conditions. The complementary slackness constraints introduced in the KKT conditions are linearized using the big-M method. The linearized model can be represented in (A4).

$$\begin{cases} \max\limits_{\boldsymbol{v} \in V, \boldsymbol{y} \in Y} \boldsymbol{v}^T \boldsymbol{y} + \varphi \\ \text{s.t.} \boldsymbol{c}^T \boldsymbol{x}^* + \boldsymbol{d}^T \boldsymbol{v} + \boldsymbol{e}^T \boldsymbol{y} \leqslant \boldsymbol{D} \\ \boldsymbol{f}^T \boldsymbol{x}^* + \boldsymbol{g}^T \boldsymbol{v} + \boldsymbol{h}^T \boldsymbol{y} + \\ \boldsymbol{i}^T \boldsymbol{u}^{*,\tau} + \boldsymbol{j}^T \boldsymbol{z}^\tau \leqslant \boldsymbol{E}, \forall \tau \leqslant n \\ \varphi \geqslant \boldsymbol{B}^T \boldsymbol{z}^\tau, \forall \tau \leqslant n \\ \boldsymbol{v}^T + \boldsymbol{\alpha} \boldsymbol{e}^T + \boldsymbol{\beta}^\tau \boldsymbol{h}^T = 0, \forall \tau \leqslant n \\ 1 - \boldsymbol{\gamma}^\tau = 0, \forall \tau \leqslant n \\ 0 \leqslant \boldsymbol{D} - \left(\boldsymbol{c}^T \boldsymbol{x}^* + \boldsymbol{d}^T \boldsymbol{v} + \boldsymbol{e}^T \boldsymbol{y} \right) \leqslant \mathrm{M} \boldsymbol{\Lambda} \\ 0 \leqslant \boldsymbol{\alpha} \leqslant \mathrm{M}(1 - \boldsymbol{\Lambda}) \\ 0 \leqslant \boldsymbol{E} - \\ \begin{pmatrix} \boldsymbol{f}^T \boldsymbol{x}^* + \boldsymbol{g}^T \boldsymbol{v} + \\ \boldsymbol{h}^T \boldsymbol{y} + \boldsymbol{i}^T \boldsymbol{u}^{*,\tau} + \boldsymbol{j}^T \boldsymbol{z}^\tau \end{pmatrix} \leqslant \mathrm{M} \boldsymbol{\sigma}^\tau, \forall \tau \leqslant n \\ 0 \leqslant \boldsymbol{\beta}^\tau \leqslant \mathrm{M}(1 - \boldsymbol{\sigma}^\tau), \forall \tau \leqslant n \\ 0 \leqslant \varphi - \boldsymbol{B}^T \boldsymbol{z}^\tau \leqslant \mathrm{M} \boldsymbol{\omega}^\tau, \forall \tau \leqslant n \\ 0 \leqslant \boldsymbol{\gamma}^\tau \leqslant \mathrm{M}(1 - \boldsymbol{\omega}^\tau), \forall \tau \leqslant n \end{cases} \tag{A4}$$

In (A4), M is a large positive value. $\boldsymbol{\Lambda}, \boldsymbol{\sigma}, \boldsymbol{\omega}$ is an introduced Boolean variable, $\boldsymbol{\alpha}, \boldsymbol{\beta}, \boldsymbol{\gamma}$ is an introduced dual variable. $\boldsymbol{n}$ represents the iteration index, φ is an introduced auxiliary variable used to link SPM and SPS, and $\boldsymbol{u}^{*,\tau}$ corresponds to the worst-case scenario of source-load obtained from SPS in the

τ-th iteration.

Furthermore, the bilinear term $\boldsymbol{v}^T\boldsymbol{y}$ can be linearized as (A5) using the strong duality theory.

$$\boldsymbol{v}^T\boldsymbol{y} = \boldsymbol{\alpha}^T\left(\boldsymbol{c}^T\boldsymbol{x}^* + \boldsymbol{d}^T\boldsymbol{v} - \boldsymbol{D}\right) + \sum_\tau \left[(\boldsymbol{\beta}^\tau)^T \begin{pmatrix} \boldsymbol{f}^T\boldsymbol{x}^* + \boldsymbol{g}^T\boldsymbol{v} + \\ \boldsymbol{i}^T\boldsymbol{u}^{*,\tau} + \boldsymbol{j}^T\boldsymbol{z}^\tau - \boldsymbol{E} \end{pmatrix} \right] + \sum_\tau \left[(\boldsymbol{\gamma}^\tau)^T\left(\boldsymbol{B}^T\boldsymbol{z}^\tau\right) \right] - \varphi \tag{A5}$$

Thus, (A4) can be transformed into (A6).

$$\begin{cases} \max\limits_{\boldsymbol{v}\in V,\boldsymbol{y}\in Y} \boldsymbol{\alpha}^T\left(\boldsymbol{c}^T\boldsymbol{x}^* + \boldsymbol{d}^T\boldsymbol{v} - \boldsymbol{D}\right) + \\ \sum_\tau \left[(\boldsymbol{\beta}^\tau)^T \begin{pmatrix} \boldsymbol{f}^T\boldsymbol{x}^* + \boldsymbol{g}^T\boldsymbol{v} + \\ \boldsymbol{i}^T\boldsymbol{u}^{*,\tau} + \boldsymbol{j}^T\boldsymbol{z}^\tau - \boldsymbol{E} \end{pmatrix} \right] + \\ \sum_\tau \left[(\boldsymbol{\gamma}^\tau)^T\left(\boldsymbol{B}^T\boldsymbol{z}^\tau\right) \right] \\ \text{s.t.} \boldsymbol{c}^T\boldsymbol{x}^* + \boldsymbol{d}^T\boldsymbol{v} + \boldsymbol{e}^T\boldsymbol{y} \leqslant \boldsymbol{D} \\ \boldsymbol{f}^T\boldsymbol{x}^* + \boldsymbol{g}^T\boldsymbol{v} + \boldsymbol{h}^T\boldsymbol{y} + \\ \boldsymbol{i}^T\boldsymbol{u}^{*,\tau} + \boldsymbol{j}^T\boldsymbol{z}^\tau \leqslant \boldsymbol{E}, \forall\tau\leqslant n \\ \varphi \geqslant \boldsymbol{B}^T\boldsymbol{z}^\tau, \forall\tau\leqslant n \\ \boldsymbol{v}^T + \boldsymbol{\alpha}\boldsymbol{e}^T + \boldsymbol{\beta}^\tau\boldsymbol{h}^T = 0, \forall\tau\leqslant n \\ 1 - \boldsymbol{\gamma}^\tau = 0, \forall\tau\leqslant n \\ 0 \leqslant \boldsymbol{D} - \left(\boldsymbol{c}^T\boldsymbol{x}^* + \boldsymbol{d}^T\boldsymbol{v} + \boldsymbol{e}^T\boldsymbol{y}\right) \leqslant \mathrm{M}\boldsymbol{\Lambda} \\ 0 \leqslant \boldsymbol{\alpha} \leqslant \mathrm{M}(1 - \boldsymbol{\Lambda}) \\ 0 \leqslant \boldsymbol{E} - \\ \begin{pmatrix} \boldsymbol{f}^T\boldsymbol{x}^* + \boldsymbol{g}^T\boldsymbol{v} + \\ \boldsymbol{h}^T\boldsymbol{y} + \boldsymbol{i}^T\boldsymbol{u}^{*,\tau} + \boldsymbol{j}^T\boldsymbol{z}^\tau \end{pmatrix} \leqslant \mathrm{M}\boldsymbol{\sigma}^\tau, \forall\tau\leqslant n \\ 0 \leqslant \boldsymbol{\beta}^\tau \leqslant \mathrm{M}(1 - \boldsymbol{\sigma}^\tau), \forall\tau\leqslant n \\ 0 \leqslant \varphi - \boldsymbol{B}^T\boldsymbol{z}^\tau \leqslant \mathrm{M}\boldsymbol{\omega}^\tau, \forall\tau\leqslant n \\ 0 \leqslant \boldsymbol{\gamma}^\tau \leqslant \mathrm{M}(1 - \boldsymbol{\omega}^\tau), \forall\tau\leqslant n \end{cases} \tag{A6}$$

(3) Derivation of SPS

$$\begin{cases} \max\limits_{\boldsymbol{u}\in U} \min\limits_{z\in Z} \boldsymbol{B}^T\boldsymbol{z} \\ \text{s.t.} \boldsymbol{f}^T\boldsymbol{x}^* + \boldsymbol{g}^T\boldsymbol{v}^* + \boldsymbol{h}^T\boldsymbol{y}^* + \\ \boldsymbol{i}^T\boldsymbol{u} + \boldsymbol{j}^T z \leqslant \boldsymbol{E} : \boldsymbol{\xi} \end{cases} \tag{A7}$$

Due to (A7) being a bi-level optimization problem, it is necessary to convert the lower-level model into upper-level constraints using the KKT conditions. The complementary relaxation constraints introduced in the KKT conditions are linearized using the big-M method. The linearized model can be represented in (A8).

$$\begin{cases} \max\limits_{\boldsymbol{u}\in U, z\in Z} \boldsymbol{B}^T\boldsymbol{z} \\ \text{s.t} \boldsymbol{f}^T\boldsymbol{x}^* + \boldsymbol{g}^T\boldsymbol{v}^* + \boldsymbol{h}^T\boldsymbol{y}^* + \\ \boldsymbol{i}^T\boldsymbol{u} + \boldsymbol{j}^T z \leqslant \boldsymbol{E} \\ \boldsymbol{B}^T + \boldsymbol{\xi}\boldsymbol{j}^T = 0 \\ 0 \leqslant \boldsymbol{E} - \\ \begin{pmatrix} \boldsymbol{f}^T\boldsymbol{x}^* + \boldsymbol{g}^T\boldsymbol{v}^* + \boldsymbol{h}^T\boldsymbol{y}^* + \\ \boldsymbol{i}^T\boldsymbol{u} + \boldsymbol{j}^T\boldsymbol{z} \end{pmatrix} \leqslant \mathrm{M}\boldsymbol{\theta} \\ 0 \leqslant \boldsymbol{\xi} \leqslant \mathrm{M}(1 - \boldsymbol{\theta}) \end{cases} \tag{A8}$$

In (A8), M is a large positive value, $\boldsymbol{\theta}$ is an introduced Boolean variable, and $\boldsymbol{\xi}$ is an introduced dual variable.

Table A1
Forecast electricity price and actual gas price.

Period of time	Time	Purchase price(￥/kWh)	Sale price(￥/kWh)	Gas price(￥/m^3)
Peak time	12:00–14:00, 19:00–22:00	1.20	0.60	2.2
Valley time	01:00–07:00, 23:00–24:00	0.40	0.20	
Usually	08:00–11:00, 15:00–18:00	0.75	0.40	

Table A2
System parameter.

α_{HES}	α_{P2H}	α_{H2P}	β_{EES}	γ_{grid}
6.5	2.57	1.55	0.5	0.8
α_{EES}	$\alpha^{e}_{\mathrm{cut}}$	$\alpha^{h}_{\mathrm{cut}}$	$P^{\mathrm{buy}}_{\mathrm{max}}$	$P^{\mathrm{sell}}_{\mathrm{max}}$
0.01	0.5	0.4	2000	2000
$\alpha^{\mathrm{CHP}}_{1}$	$\alpha^{\mathrm{CHP}}_{2}$	$\alpha^{\mathrm{CHP}}_{3}$	$\alpha^{\mathrm{CHP}}_{4}$	$\alpha^{\mathrm{CHP}}_{5}$
3.021	0.9919	6.063	0.5002	1.487
$\alpha^{\mathrm{CHP}}_{6}$	$\alpha^{\mathrm{CHP}}_{7}$	$P^{\mathrm{CHP}}_{e,max}$	$\alpha^{\mathrm{EHM}}_{1}$	$\alpha^{\mathrm{EHM}}_{2}$
0.4933	0.85	3000	0.04086	35.46
$P^{\mathrm{P2H}}_{\mathrm{min}}$	$P^{\mathrm{P2H}}_{\mathrm{max}}$	$P^{\mathrm{H2P}}_{\mathrm{min}}$	$P^{\mathrm{H2P}}_{\mathrm{max}}$	$\rho_{\mathrm{H_2}}$
100	1000	100	1000	0.0899
$S^{\mathrm{HES}}_{\mathrm{min}}$	$S^{\mathrm{HES}}_{\mathrm{max}}$	α^{GB}	$P^{\mathrm{GB}}_{h,max}$	$P^{\mathrm{ch}}_{\mathrm{max}}$
90	270	8.73	3000	300
$P^{\mathrm{dis}}_{\mathrm{max}}$	$b_{\mathrm{CO_2}}/(\mathrm{kg/kW})$	η_{dis}	$S^{\mathrm{EES}}_{\mathrm{min}}$	$S^{\mathrm{EES}}_{\mathrm{max}}$
300	0.95	0.95	300	900
$P^{e}_{ij,min}$	$P^{e}_{ij,max}$	$p^{\mathrm{tran}}_{ij,min}$	$p^{\mathrm{tran}}_{ij,max}$	β^{e}_{cut}
−200	200	−200	200	0.15
β^{h}_{cut}	$p^{\mathrm{load}}_{i,max}$	$h^{\mathrm{load}}_{i,max}$		
0.15	1000	1000		

Table A3
Algorithm parameter.

ε_1	ε_2	$\boldsymbol{v}^{*,0}$	$\boldsymbol{u}^{*,0}$	ε_3
0.01	0.01	$\widehat{\boldsymbol{p}}^{\mathrm{buy}}$、$\widehat{\boldsymbol{p}}^{\mathrm{sell}}$	$\widehat{\boldsymbol{P}}^{\mathrm{WT}}$、$\widehat{\boldsymbol{P}}^{\mathrm{PV}}$、$\widehat{\boldsymbol{P}}_{e}^{\mathrm{load}}$、$\widehat{\boldsymbol{P}}_{h}^{\mathrm{load}}$	0.01
ε_4	$\rho_{ij,1}$	$\boldsymbol{\lambda}^{0}_{ij,1}$	$\boldsymbol{P}^{e,0}_{ij}$	ε_4
0.01	0.01	0	0	0.01
$\rho_{ij,2}$	$\boldsymbol{\lambda}^{0}_{ij,2}$	$\boldsymbol{p}^{e,0}_{ij}$	ε_5	$\rho_{ij,3}$
10	0	0	0.01	10
$\boldsymbol{\lambda}^{0}_{ij,3}$	$\boldsymbol{p}^{e,\mathrm{tran},0}_{ij}$			
0	0			

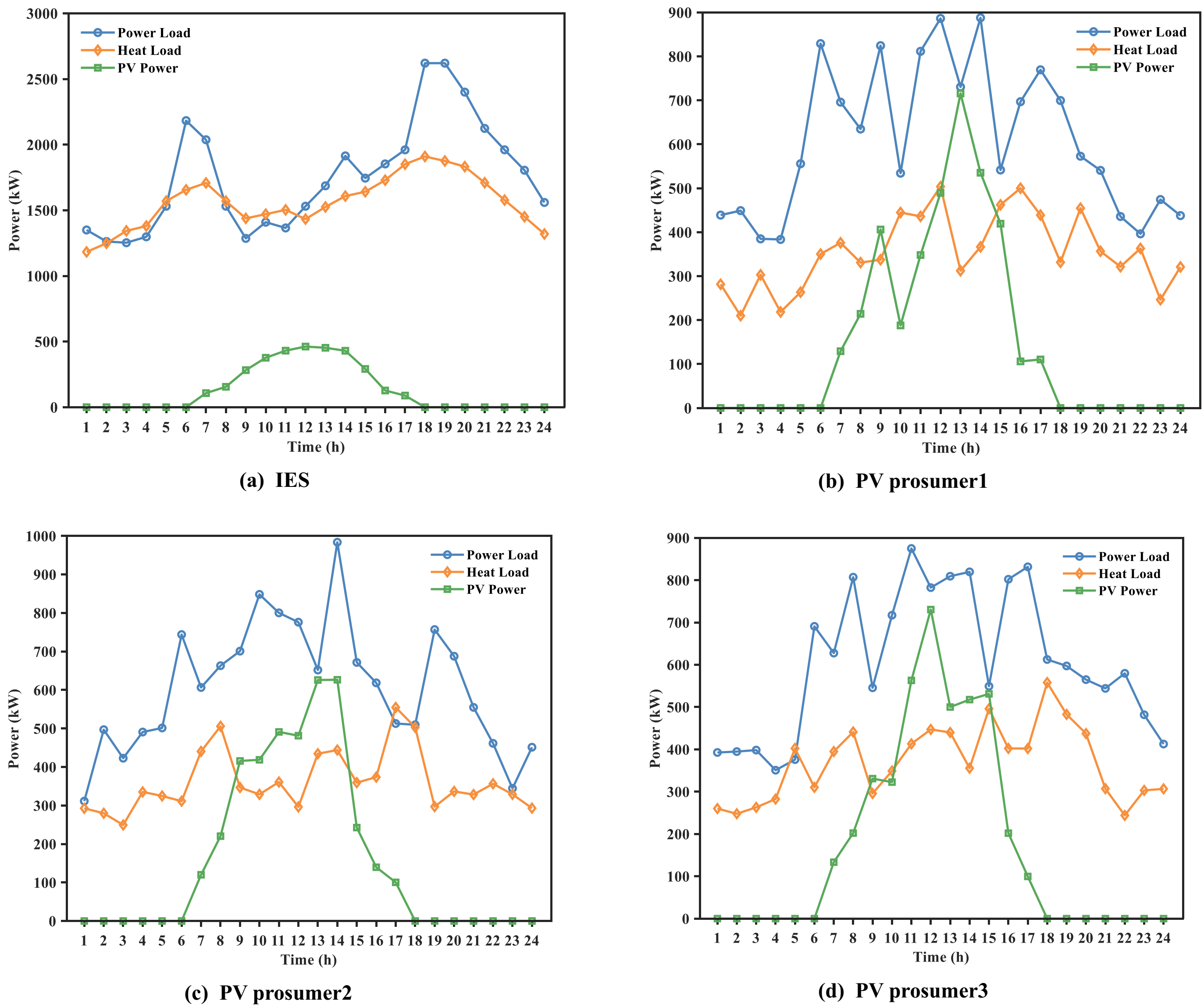
Power Load
Heat Load
PV Power
Power (kW)
Time (h)
(a) IES
(b) PV prosumer1
(c) PV prosumer2
(d) PV prosumer3

Fig. A1. IES1.

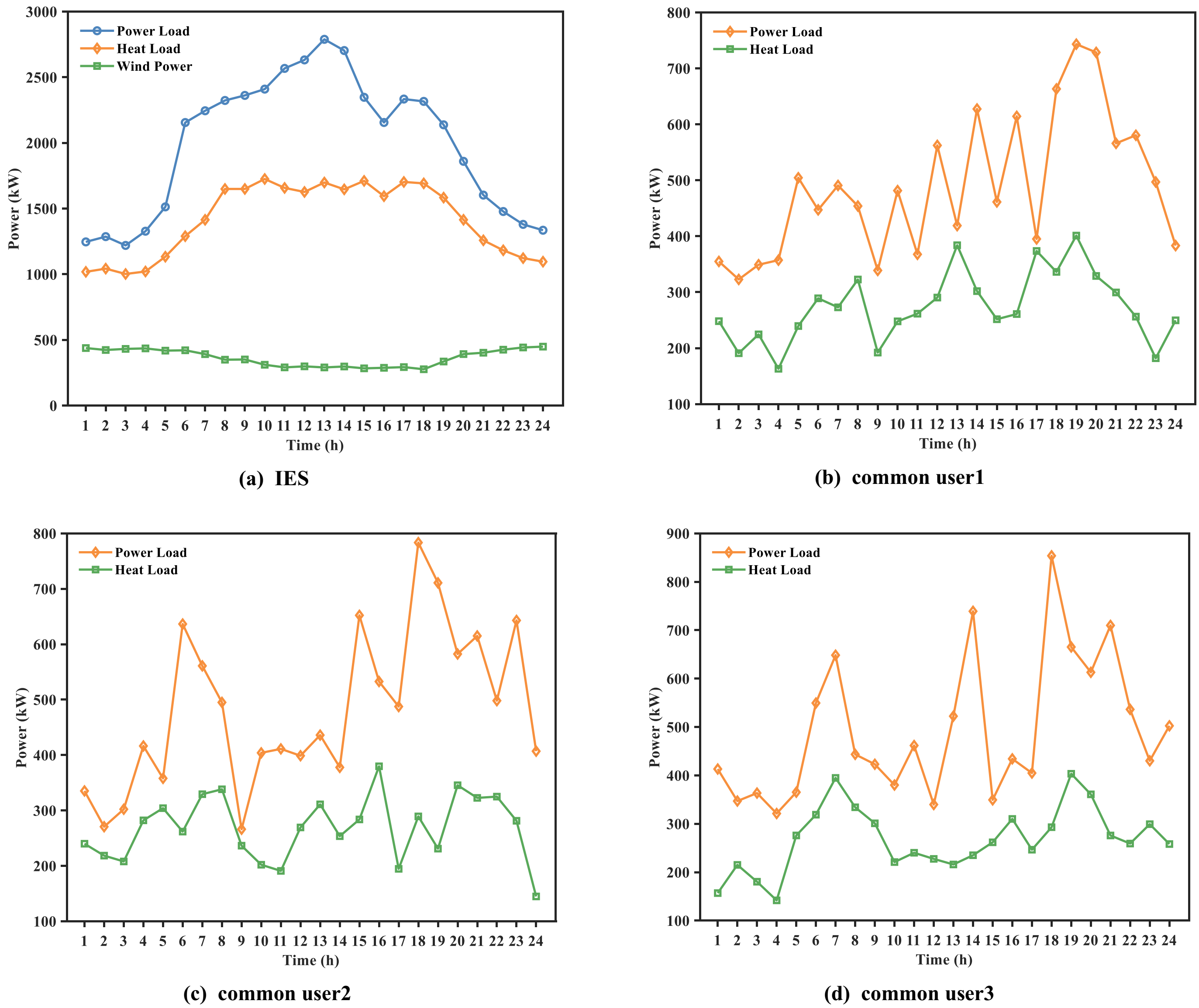
Power Load
Heat Load
Wind Power
Power (kW)
Time (h)
(a) IES
Power Load
Heat Load
Power (kW)
Time (h)
(b) common user1
Power Load
Heat Load
Power (kW)
Time (h)
(c) common user2
Power Load
Heat Load
Power (kW)
Time (h)
(d) common user3

Fig. A2. IES2.

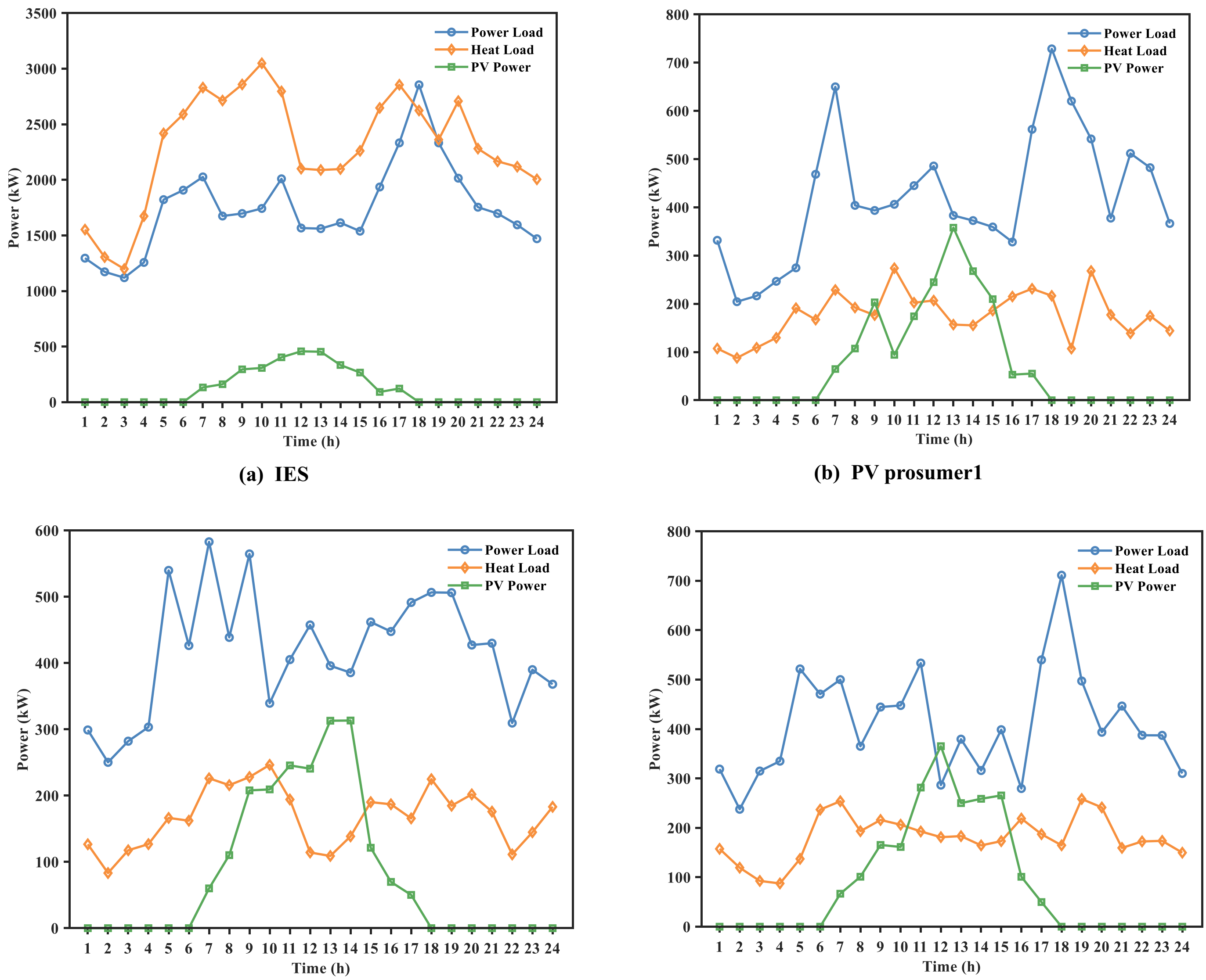

(a) IES

(b) PV prosumer1

(c) PV prosumer2

(d) PV prosumer3

Fig. A3. IES3

Appendix B. Appendix

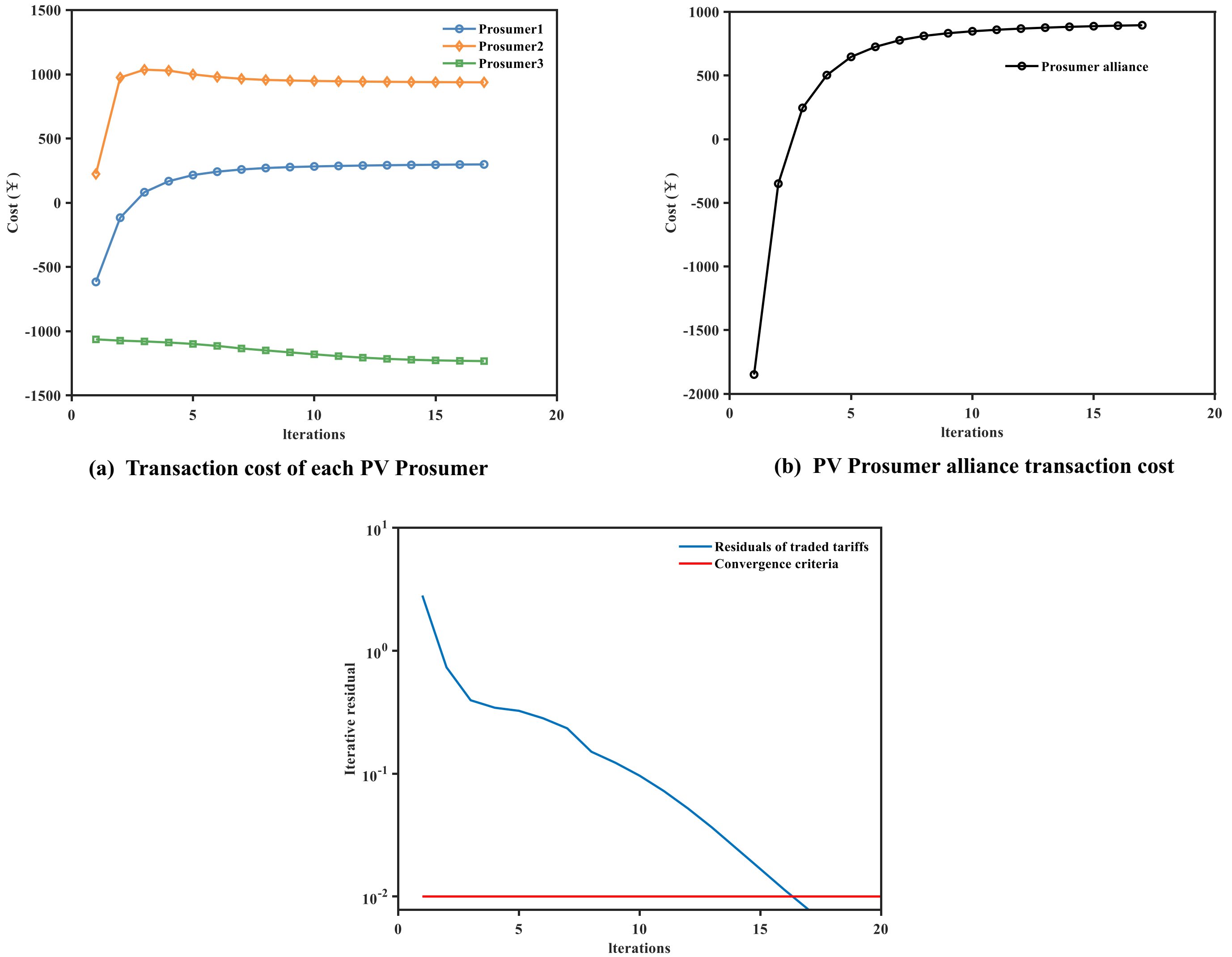

(a) Transaction cost of each PV Prosumer

(b) PV Prosumer alliance transaction cost

(c) Residual

Fig. B1. P2 distributed iterative convergence of PV prosumer inside IES1.

The ADMM algorithm was employed to solve P2, yielding the convergence curves of transaction costs and residual errors for each PV prosumer and PV prosumer alliance, as shown in Fig. B1. Due to the small scale of the problem, the convergence criterion for transaction price residuals was met after 17 iterations. The transaction costs for each PV prosumer converged to their optimal values of 297.34 ¥, 935.35 ¥, and − 1232.58 ¥, respectively. During the iterations, these transaction costs exhibited some fluctuations, reflecting the bargaining process among the three PV prosumers. The corresponding transaction costs for the PV prosumer alliance converged to an optimal value of 0.11 ¥, which is close to zero, indicating the internal balance of energy transactions. The computational time for solving the model algorithm was 22.5 s.

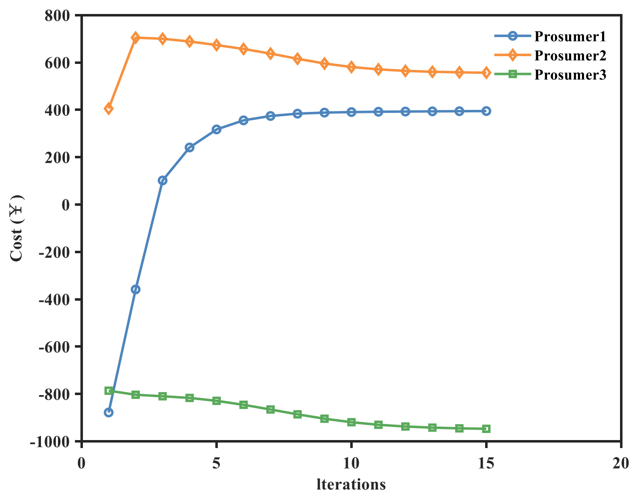

(a) Transaction cost of each PV Prosumer

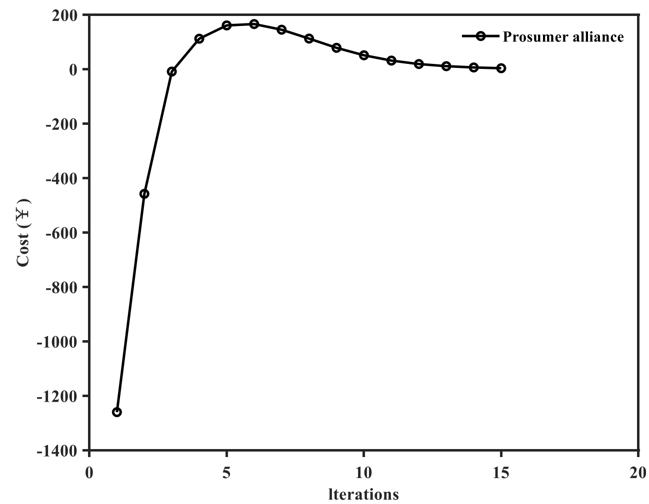

(b) PV Prosumer alliance transaction cost

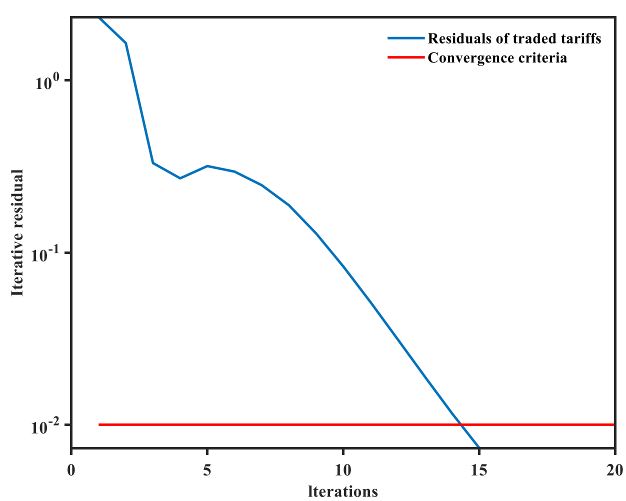

(c) Residual

Fig. B2. P2 distributed iterative convergence of PV prosumer inside IES3.

The ADMM algorithm was utilized to solve P2, resulting in the convergence curves of transaction costs and residual errors for each PV prosumer and PV prosumer alliance, as illustrated in Fig. B2. Due to the relatively small scale of the problem, the convergence criterion for transaction price residuals was achieved after 15 iterations. The transaction costs for each PV prosumer converged to their optimal values of 392.73 ¥, 554.62 ¥, and −947.14 ¥, respectively. Throughout the iterations, these transaction costs exhibited some fluctuations, reflecting the bargaining process among the three PV prosumers. The corresponding transaction costs for the PV prosumer alliance converged to an optimal value of 0.21 ¥, which closely approached zero, thus reflecting the internal equilibrium of energy trading. The computational time for solving the model algorithm was 14.9 s.

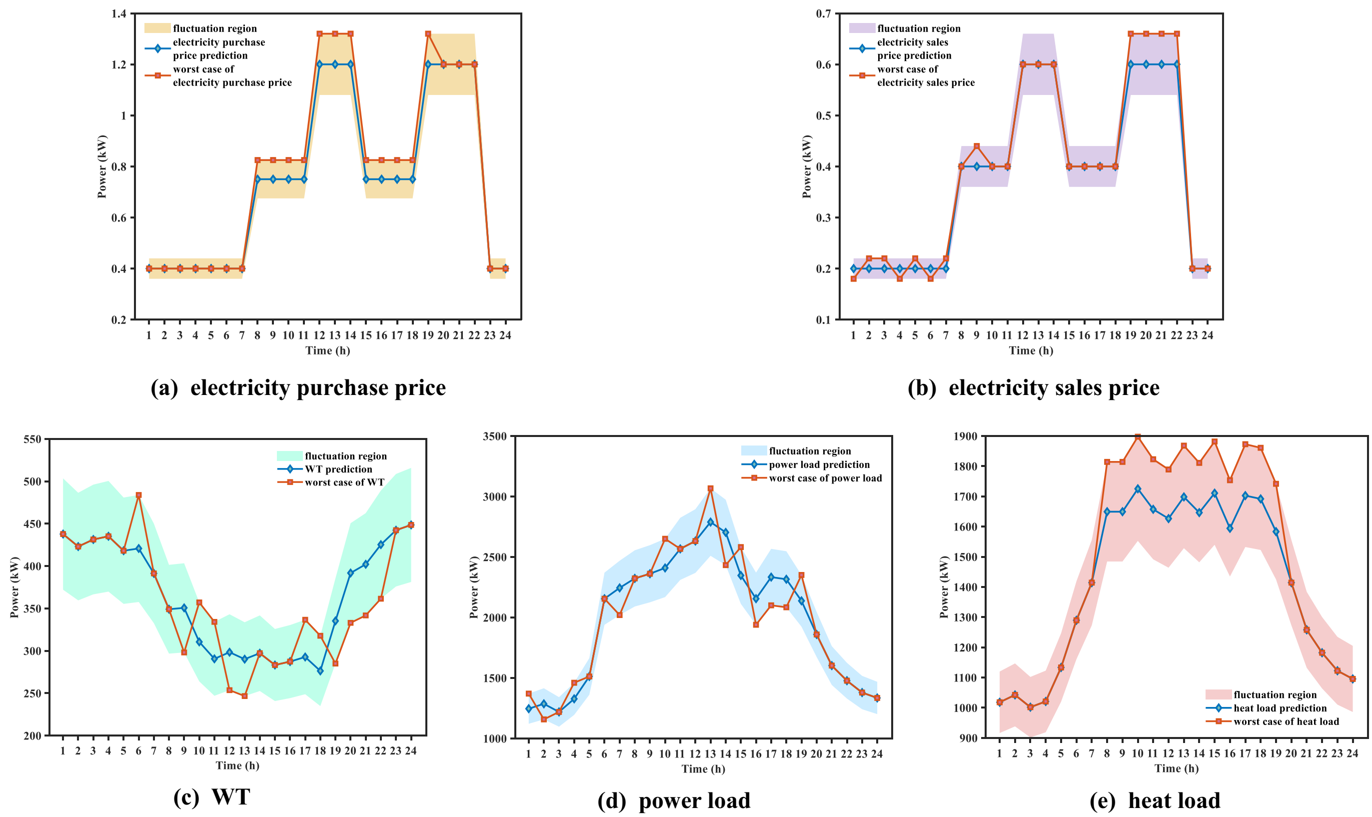

Fig. B3. Worst case of IES2.

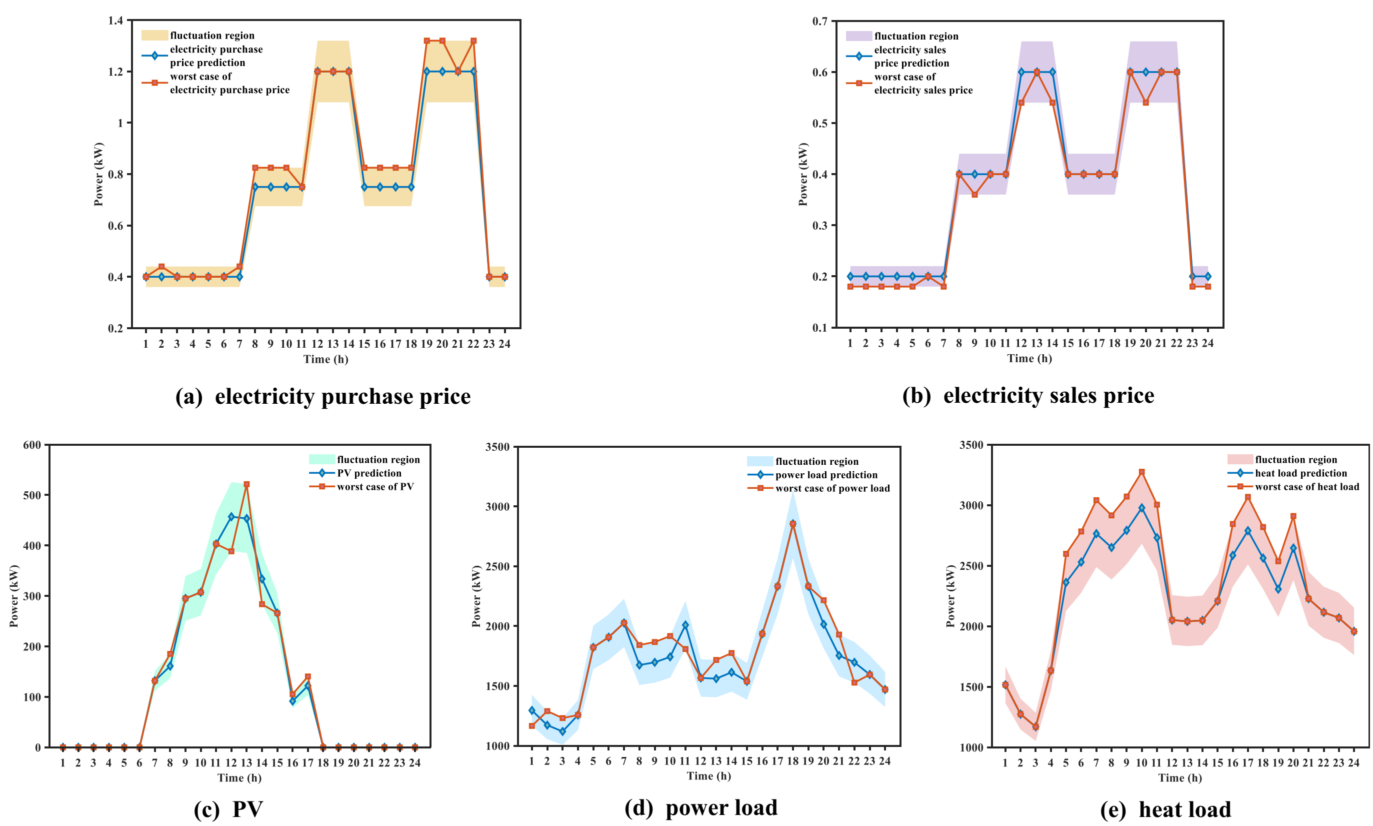

Fig. B4. Worst case of IES3.

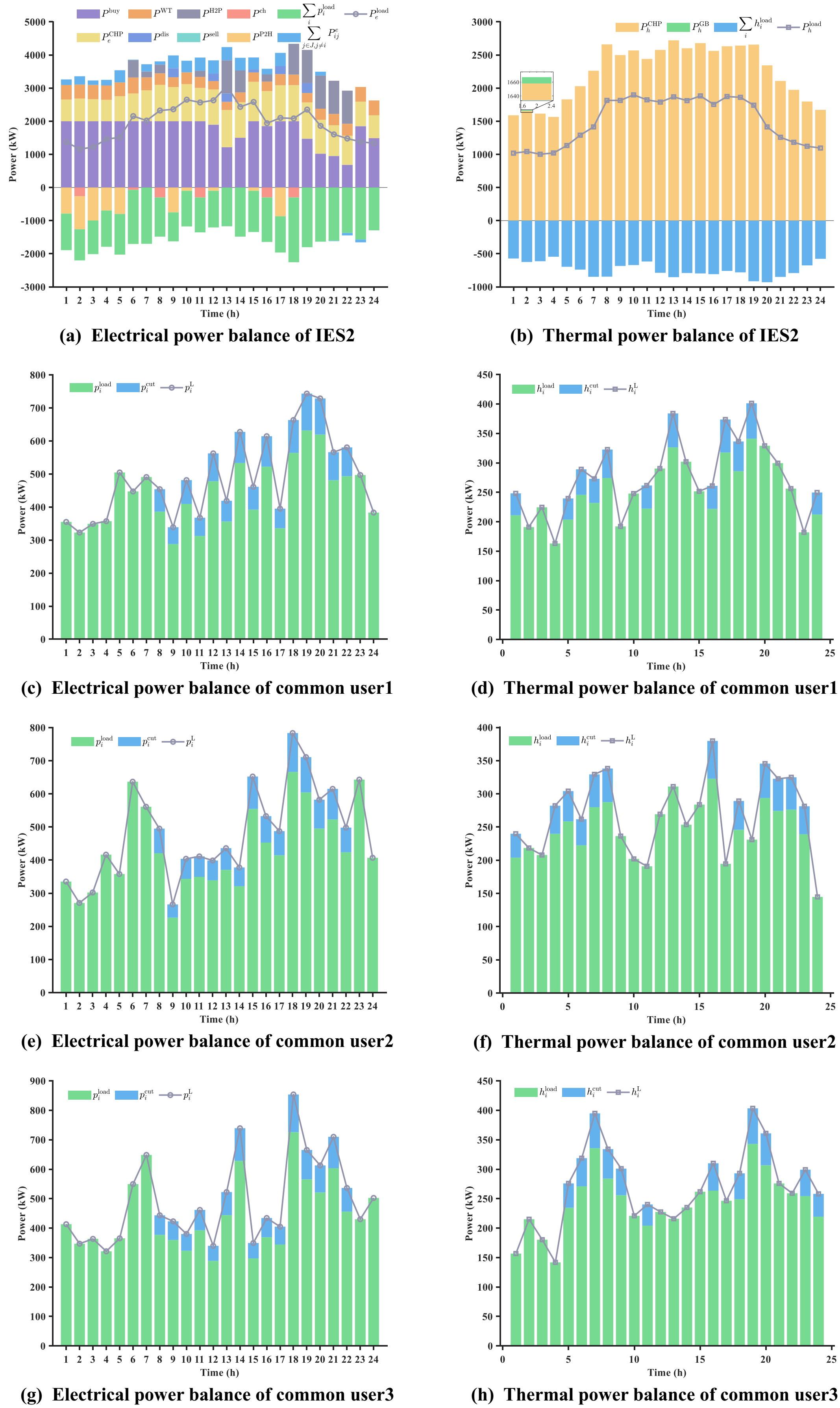

(a) Electrical power balance of IES2
(b) Thermal power balance of IES2
(c) Electrical power balance of common user1
(d) Thermal power balance of common user1
(e) Electrical power balance of common user2
(f) Thermal power balance of common user2
(g) Electrical power balance of common user3
(h) Thermal power balance of common user3

Fig. B5. Energy balance of IES2.

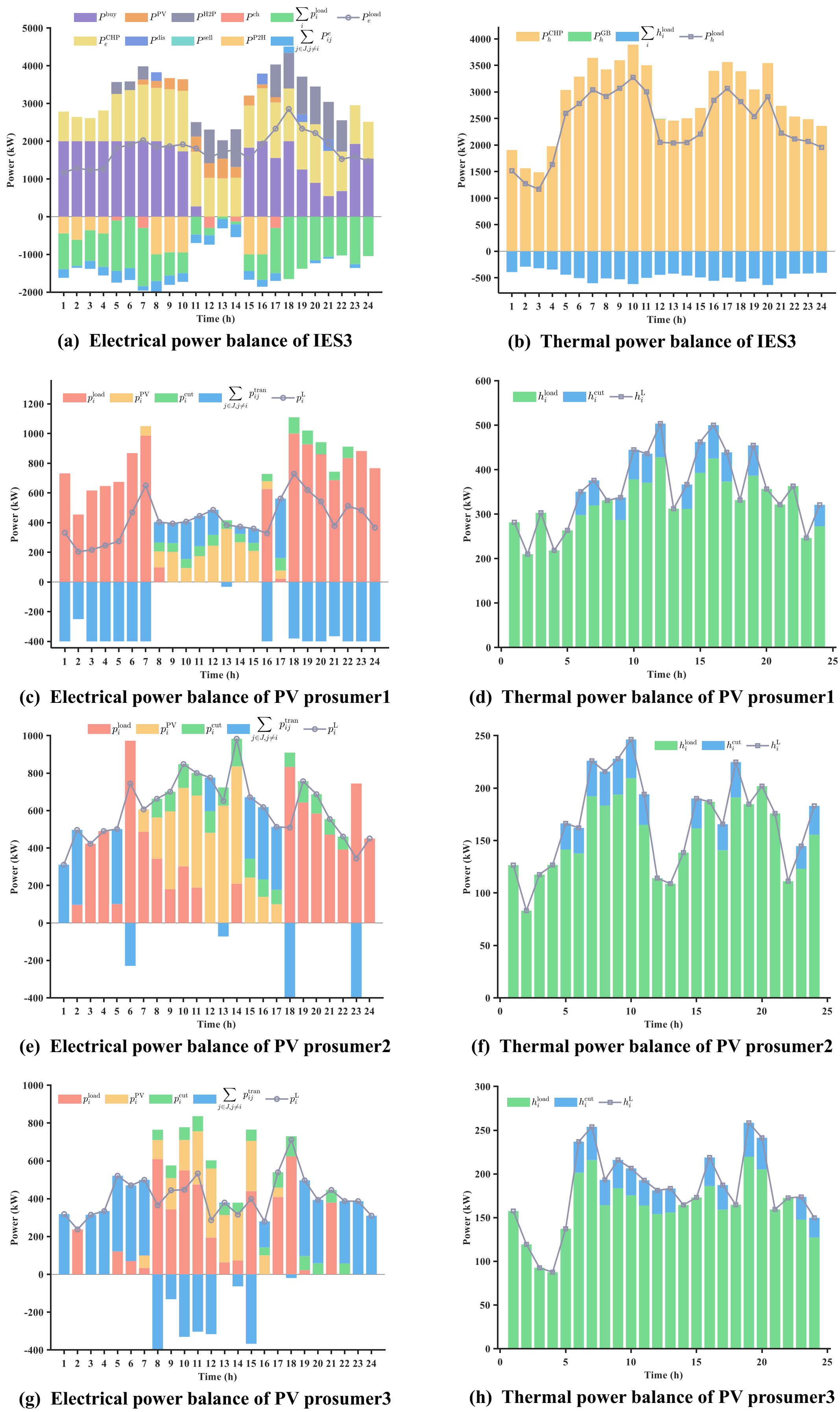

(a) Electrical power balance of IES3
(b) Thermal power balance of IES3
(c) Electrical power balance of PV prosumer1
(d) Thermal power balance of PV prosumer1
(e) Electrical power balance of PV prosumer2
(f) Thermal power balance of PV prosumer2
(g) Electrical power balance of PV prosumer3
(h) Thermal power balance of PV prosumer3

Fig. B6. Energy balance of IES3.

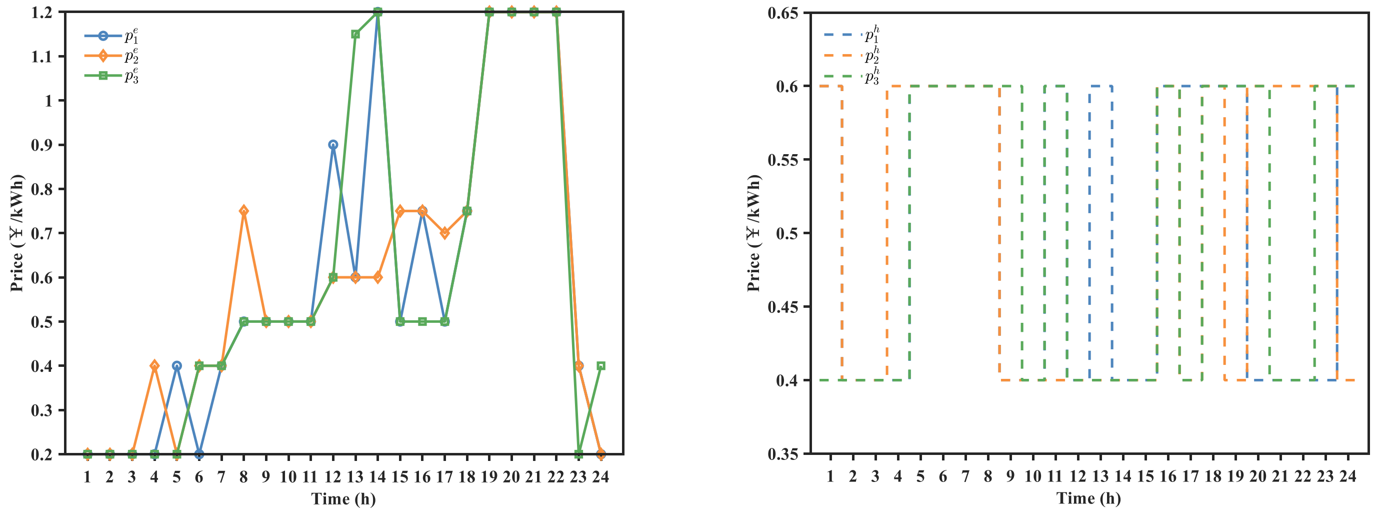

(a) electricity price **(b) heat price**

Fig. B7. Stackelberg game energy transaction price of IES2.

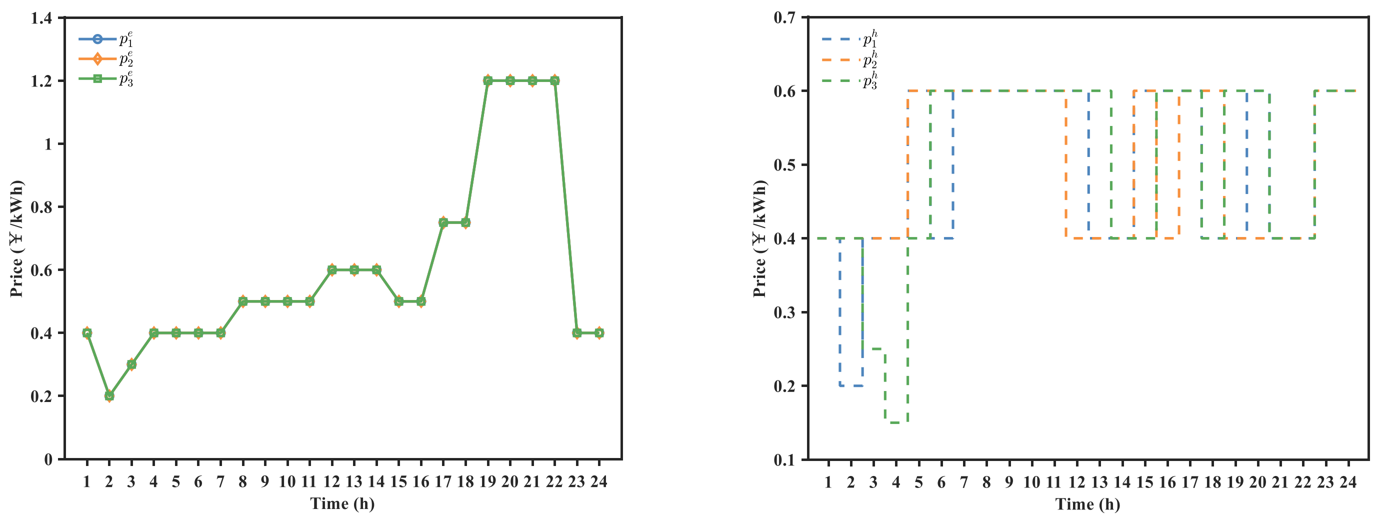

(a) electricity price **(b) heat price**

Fig. B8. Stackelberg game energy transaction price of IES3.

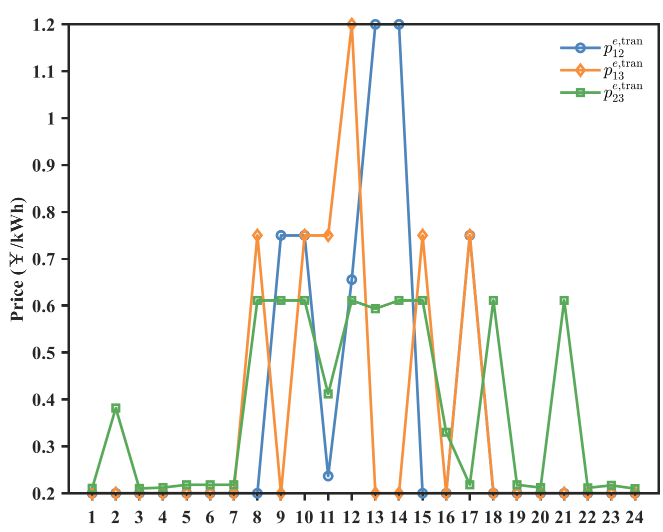

Fig. B9. Transaction electricity price results between PV prosumers within IES3.

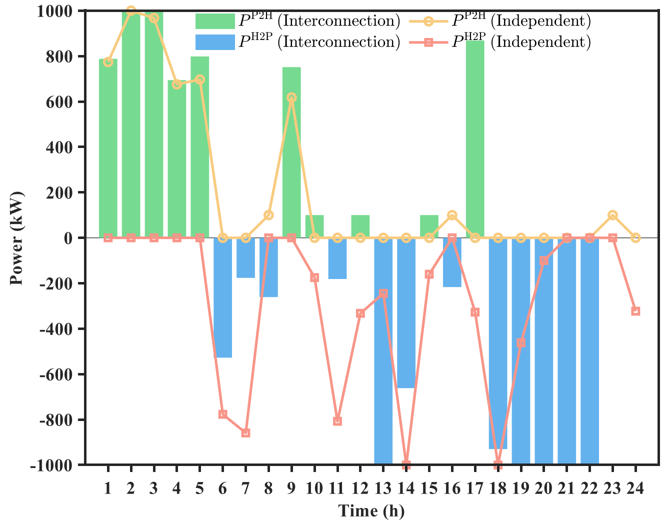

Fig. B10. EHM scheduling plan for IES2.

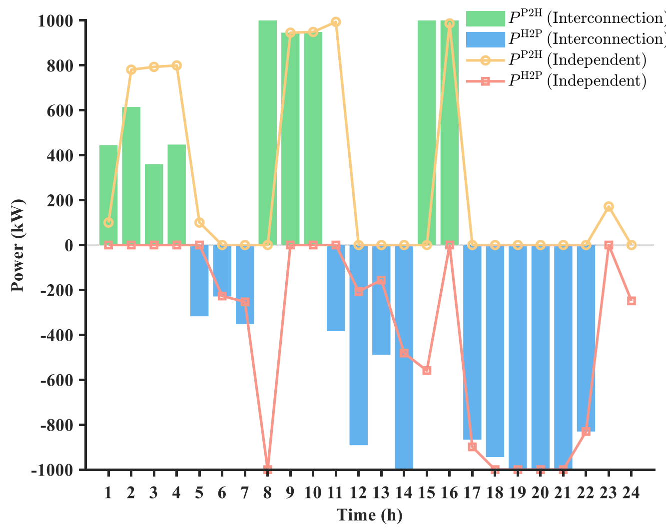

Fig. B11. EHM scheduling plan for IES3.

Table B1
Pre- and post-transaction settlement costs for each PV prosumer within IES1.

Cost	PV Prosumer1	PV Prosumer2	PV Prosumer3	PV Prosumer alliance
Independent operation cost/$	13,637.04	11,486.73	8006.84	33,130.61
Interconnection operation without transaction cost/$	12,982.34	10,201.48	9042.76	32,226.58
Transaction cost/$	297.34	935.35	−1232.58	0.11
Final cost of interconnection operation/$	13,279.68	11,136.83	7810.18	32,229.69
Cost reduction value/$	357.36	349.90	196.66	903.92

Table B2
Pre- and post-transaction settlement costs for each PV prosumer within IES3.

Cost	PV Prosumer1	PV Prosumer2	PV Prosumer3	PV Prosumer alliance
Independent operation cost/$	11,051.73	6227.54	4729.32	22,008.59
Interconnection operation without transaction cost/$	10,253.54	5462.34	5468.74	21,184.62
Transaction cost/$	392.73	554.62	−947.14	0.21
Final cost of interconnection operation/$	10,646.27	6016.96	4521.60	21,188.83
Cost reduction value/$	405.46	210.58	207.72	823.76

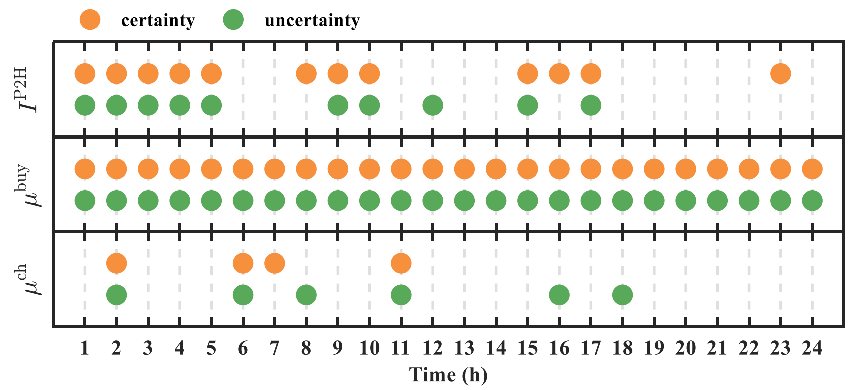

Fig. B12. Comparison of state variables of IES2 scheduling operation plan.

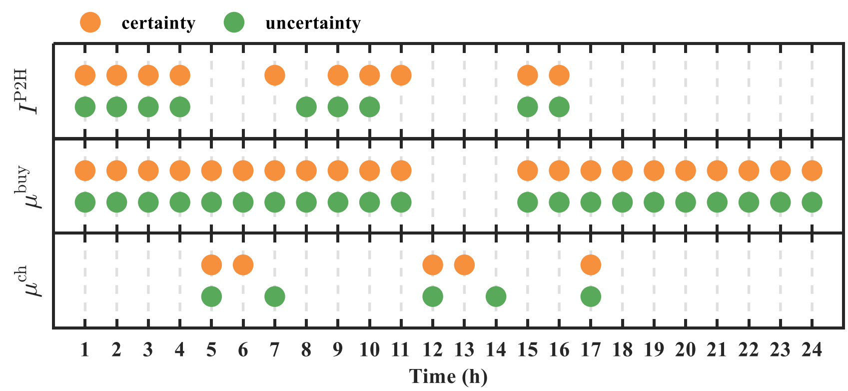

Fig. B13. Comparison of state variables of IES3 scheduling operation plan.

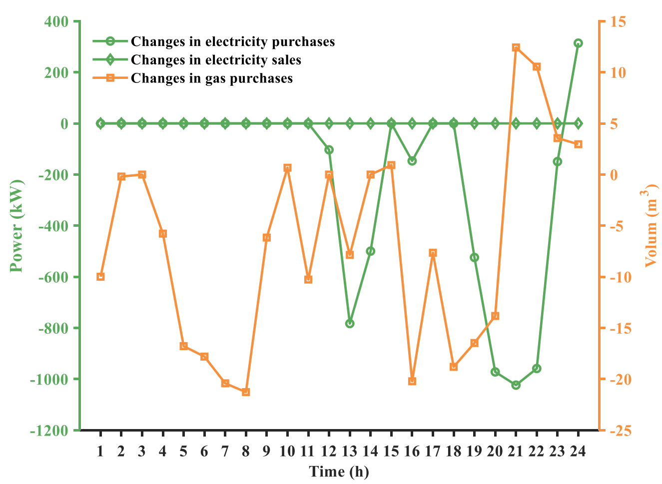

Fig. B14. Changes in the power of the external energy port of IES2.

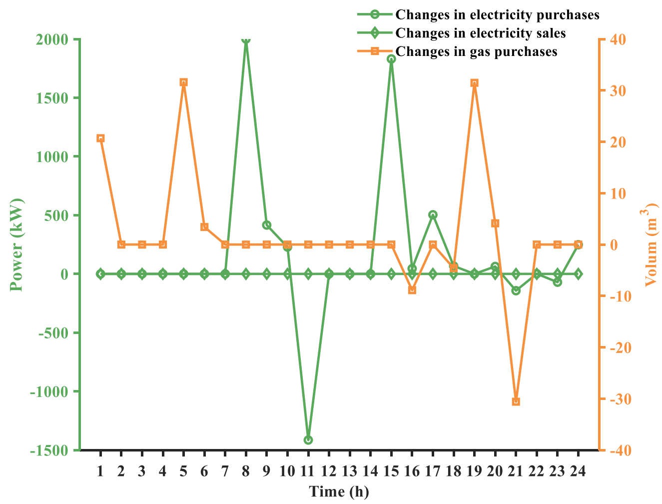

Fig. B15. Changes in the power of the external energy port of IES3.

References

[1] Li Lin, Xinyao Zheng, Longwen Zhou. Wind-PV-thermal-storage multi-energy complementary optimal dispatching based on hydrogen gas turbine[J]. Power Syst Technol 2022;46(8):3007–22. https://doi.org/10.13335/j.1000-3673.pst.2022.0059.

[2] Li JR, Lin J, Zhang HC, et al. Optimal investment of electrolyzers and seasonal storages in hydrogen supply chains incorporated with renewable electric networks [J]. IEEE Trans Sustain Energy 2020;11(3):1773–84. https://doi.org/10.1109/TSTE.2019.2940604.

[3] Fang X, Wang Y, Dong W, et al. Optimal energy management of multiple electricity-hydrogen integrated charging stations. Energy 2023;262:125624. https://doi.org/10.1016/j.energy.2022.125624.

[4] Dengyong Chen, Fang Liu, Shuai Liu. Optimization of virtual power plant scheduling coupling with P2G-CCS and doped with gas hydrogen based on stepped carbon trading[J]. Power Syst Technol 2022;46(6):2042–53. https://doi.org/10.13335/j.1000-3673.pst.2021.2177.

[5] Hao Wang, Jianwei Huang. Incentivizing energy trading for interconnected microgrids. IEEE Trans Smart Grid July 2018;9(4):2647–57. https://doi.org/10.1109/TSG.2016.2614988.

[6] Mingyong Cui, Mingyang Xuan, Zhigang Lu, et al. Operation optimization strategy of multi integrated energy service companies based on cooperative game theory[J]. Proc CSEE 2022;42(10):3548–64. https://doi.org/10.13334/j.0258-8013.pcsee.202163.

[7] Qi Wang, Ning Ll, Xin Gu, et al. Optimization strategy for cooperative operation of integrated energy service providers considering carbon emission reduction[J]. Automat Electric Power Syst 2022;46(7):131–40. https://doi.org/10.7500/AEPS20210606002.

[8] Yinbo Zhao, Hongjun Gao, Zhong Wang, et al. Optimal decision of multi-energy trading with game for commercial park operators considering user-side electricity substitution[J]. Power Syst Technol 2021;45(4):1320–31. https://doi.org/10.13335/j.1000-3673.pst.2020.1599.

[9] Sorin E, Bobo L, Pinson P. Consensus-based approach to peer-to-peer electricity markets with product differentiation[J]. IEEE Trans Power Syst 2019;34(2):994–1004. https://doi.org/10.1109/TPWRS.2018.2872880.

[10] Xingan Yao, Wenhao Liu, Xueliang Gong, Jiaxun Liu, Wenjun Zhu, Jianquan Zhu. A fully decentralized clearing method for peer-to-peer trading of prosumers based on improved dual dynamic programming[J]. Power Syst Technol 2023−10−01:1–12. https://doi.org/10.13335/j.1000-3673.pst.2023.0512.

[11] Dongfeng Ang, et al. Source-storage configuration for user-side integrated energy system based on interval linear programming[J]. Power Syst Technol 2022;46(06):2064–76. https://doi.org/10.13335/j.1000-3673.pst.2021.2260.

[12] Yang Lei, et al. Multi-stage rolling stochastic planning of regional integrated energy system considering dual-uncertainty[J]. Automat Electric Power Syst 2023;47(20):53–63. https://doi.org/10.7500/AEPS20230423002.

[13] Zhi Qiu, Beibei Wang, Shujun Ben, et al. Bi-level optimal configuration planning model of regional integrated energy system considering uncertainties[J]. Electric Power Automat Equip 2019;39(8):176–85. https://doi.org/10.16081/j.epae.201908005.

[14] Zhang H, Chen Y, Liu K, et al. A novel power system scheduling based on hydrogen-based micro energy hub[J]. Energy 2022;251:123623. https://doi.org/10.1016/j.energy.2022.123623.

[15] Mansour-Saatloo A, Agabalaye-Rahvar M, Mirzaei MA, et al. Robust scheduling of hydrogen based smart micro energy hub with integrated demand response[J]. J Clean Prod 2020;267:122041. https://doi.org/10.1016/j.jclepro.2020.122041.

[16] Yixin Liu, Li Guo, Chengshan Wang. Economic dispatch of microgrid based on two stage robust optimization[J]. Proc CSEE 2018;38(14):4013–22. https://doi.org/10.13334/j.0258-8013.pcsee.170500.

[17] Ma Haotian, Hu Junjie, Yuxuan Tong. A two-stage robust planning approach for data center microgrids considering flexibility [J]. Proc CSEE 2022:1–13. https://doi.org/10.13334/j.0258-8013.pcsee.221146.

[18] Jiang AH, Yuan HH, Li DL. Energy management for a community-level integrated energy system with photovoltaic prosumers based on bargaining theory. Energy 2021;225:120272. https://doi.org/10.1016/j.energy.2021.120272.

[19] Li Z, Wu L, Xu Y, et al. Distributed tri-layer risk-averse stochastic game approach for energy trading among multi-energy microgrids. Appl Energy 2023;331:120282. https://doi.org/10.1016/j.apenergy.2022.120282.

[20] Lu S, et al. Unlock the thermal flexibility in integrated energy systems: a robust nodal pricing approach for thermal loads. IEEE Trans Smart Grid July 2023;14(4):2734–46. https://doi.org/10.1109/TSG.2023.3258441.

[21] Qiu H, Gu W, Wang L, Pan G, Xu Y, Wu Z. Trilayer Stackelberg game approach for robustly power management in community grids. IEEE Trans Industr Inform June 2021;17(6):4073–83. https://doi.org/10.1109/TII.2020.3015733.

[22] Qiu H, Gooi HB, Gao H, Veerasamy V, Li Y. Cooperative power bidding of smart community grids with an aggregator-prosumer-based hierarchical framework. IEEE Trans Smart Grid July 2023;14(4):3032–45. https://doi.org/10.1109/TSG.2022.3230510.

[23] Lei Zhong, Hongjun Gao, Yanhong Yang, et al. Load peak shaving operation management and control strategy of AC/DC hybrid distribution network based on two-stage robust game model[J]. Proc CSEE 2022;42(15):5550–6. https://doi.org/10.13334/j.0258-8013.pcsee.210628.

[24] Cao X, Cao T, Xu Z, Zeng B, Gao F, Guan X. Resilience constrained scheduling of mobile emergency resources in electricity-hydrogen distribution network. IEEE Trans Sustain Energy April 2023;14(2):1269–84. https://doi.org/10.1109/TSTE.2022.3217514.

[25] Yachao Zhang, Feng Zheng, Jian Le, et al. A distributionally robust coordinated optimization scheduling of integrated electricity and natural gas systems considering higher-order uncertainty of wind power[J]. Proc CSEE 2020;40(24). https://doi.org/10.13334/j.0258-8013.pcsee.191354. 8012–8026+8238.